Compositions of dikes and lavas from the Pito Deep Rift: Implications for crustal accretion at superfast spreading centers

Meagen A. Pollock,[1] Emily M. Klein,[2] Jeffrey A. Karson,[3] and Drew S. Coleman[4]

Received 12 October 2007; revised 13 December 2008; accepted 12 January 2009; published 19 March 2009.

[1] The northwest trending walls of the Pito Deep Rift (PDR), a tectonic window in the southeast Pacific, expose in situ oceanic crust generated ~3 Ma at the superfast spreading southern East Pacific Rise (SEPR). Whole rock analyses were performed on over 200 samples of dikes and lavas recovered from two ~8 km^2 study areas. Most of the PDR samples are incompatible-element-depleted normal mid-ocean ridge basalts (NMORB; $(La/Sm)_N < 1.0$) that show typical tholeiitic fractionation trends. Correlated variations in Pb isotope ratios, rare earth element patterns, and ratios of incompatible elements (e.g., $(Ce/Yb)_N$) are best explained by mixing curves between two enriched and one depleted mantle sources. Pb isotope compositions of most PDR NMORB are offset from SEPR data toward higher values of $^{207}Pb/^{204}Pb$, suggesting that an enriched component of the mantle was present in this region in the past ~3 Ma but is not evident today. Overall, the PDR crust is highly variable in composition over long and short spatial scales, demonstrating that chemically distinct lavas and dikes can be emplaced within the same segment over short timescales. However, the limited spatial distribution of high $^{206}Pb/^{204}Pb$ samples and the occurrence of relatively homogeneous MgO compositions (ranging <2.5 wt %) within a few of the individual dive transects (over distances of ~1 km) suggests that the mantle source composition evolved and magmatic temperatures persisted over timescales of tens of thousands of years. The high degree of chemical variability between pairs of adjacent dikes is interpreted as evidence for along-axis transport of magma from chemically distinct portions of the melt lens. Our findings suggest that lateral dike propagation occurs to a significant degree at superfast spreading centers.

Citation: Pollock, M. A., E. M. Klein, J. A. Karson, and D. S. Coleman (2009), Compositions of dikes and lavas from the Pito Deep Rift: Implications for crustal accretion at superfast spreading centers, *J. Geophys. Res.*, *114*, B03207, doi:10.1029/2007JB005436.

1. Introduction

[2] Much of our understanding of the processes that lead to the accretion of the ocean crust depends on seafloor observations, remote geophysical surveys, drill cores, and comparisons to ophiolite complexes. Each of these approaches has provided valuable insights into the processes of crustal accretion, but each also has limitations. Direct observations of the seafloor, by submersible, remotely operated vehicle or other photographic or sonar imaging provide information only on the surface carapace of the seafloor. Geophysical investigations, such as seismic or gravity surveys of the neovolcanic zone, can place important constraints on the internal structure of a ridge system, but often yield seismically defined layering that is difficult to correlate with crustal geology [e.g., *Christeson et al.*, 2007]. Drill cores offer an opportunity to validate geophysical investigations as well as sample in situ oceanic crust with depth, but are limited by their one-dimensional nature.

[3] Significant contributions to our understanding of crustal accretion have been made recently through studies of "tectonic windows," faulted escarpments that expose extensive sections of the oceanic lithosphere. As a complement to drilling and ophiolites, tectonic windows provide direct access to in situ ocean crust without the questions of provenance that plague ophiolite studies. In contrast to seafloor investigations, tectonic windows offer the opportunity to sample the ocean crust with depth at spatial scales that rival terrestrial sampling. Observations from tectonic windows in the northeast Pacific (Blanco Transform), equatorial Pacific (Hess Deep Rift), and southeast Pacific (Endeavor Deep Rift) reveal that the architecture and composition of the upper crust at intermediate to superfast rate spreading centers are more complicated than predicted by current models for crustal accretion [*Tivey et al.*, 1998; *Karson et al.*, 2002a, 2002b; *Stewart et al.*, 2002; *Stewart et al.*, 2003; *Larson et al.*, 2005; *Pollock et al.*, 2005].

[1]Department of Geology, College of Wooster, Wooster, Ohio, USA.
[2]Division of Earth and Ocean Sciences, Duke University, Durham, North Carolina, USA.
[3]Department of Earth Sciences, Syracuse University, Syracuse, New York, USA.
[4]Department of Geological Sciences, University of North Carolina at Chapel Hill, Chapel Hill, North Carolina, USA.

0148-0227/09/2007JB005436$09.00

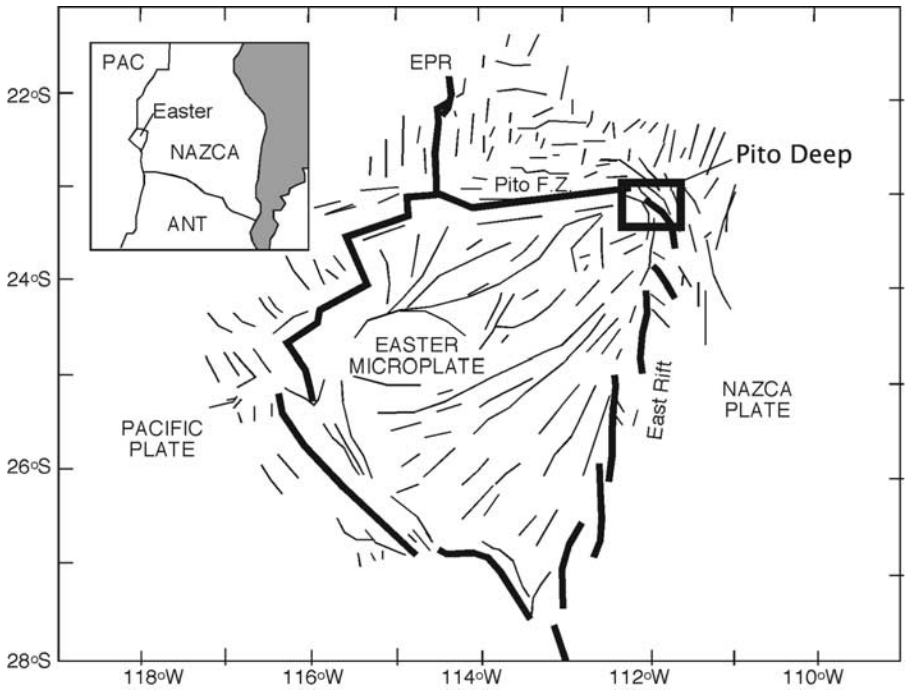

Figure 1. Structural interpretation of the Easter Microplate region (modified after *Naar and Hey* [1991]). The Pito Deep Rift, located on the northeast corner of the Easter Microplate, cuts across Nazca Plate crust originally created near 23°S on the East Pacific Rise (EPR). Box encompasses study areas A and B.

[4] This study presents chemical analyses of dikes and lavas from the Pito Deep Rift (PDR), a tectonic window in the southeast Pacific that exposes ocean crust generated at a superfast spreading center. The steep walls of the PDR expose continuous (~5 km wide) and intact sections of ocean crust, from the uppermost lavas down into the dikes and the underlying gabbroic unit. Prior to this investigation, information on crust formed at superfast spreading rates was primarily derived from marine studies along the southern East Pacific Rise (SEPR; 13°S–23°S), a region currently spreading at a rate greater than 140 mm/a [*Sempéré et al.*, 1987; *Sinton et al.*, 1991; *Bach et al.*, 1994; *Mahoney et al.*, 1994; *Cormier and Macdonald*, 1994; *Sinton et al.*, 2002]. Recently, Ocean Drilling Program (ODP) Hole 1256D penetrated over 1500 m deep into crust formed at superfast spreading rates up to 200 mm/a [*Wilson et al.*, 2006]. Our work at the PDR compliments these studies, providing an additional perspective on superfast spreading crust that is unattainable by other approaches. An examination of the compositions of dikes and lavas from the PDR reveals systematic patterns that lead to a better understanding of the temporal and spatial scales of crustal accretion processes at superfast rate spreading centers.

2. Geologic Setting and Investigation of the Pito Deep Rift

[5] The Pito Deep Rift (PDR), located at the northeast corner of the Easter Microplate in the southeast Pacific Ocean (23°S, 112°W; Figure 1) is characterized by a wide zone of deformation produced by the northwesterly propagation of the East Rift of the microplate into old Nazca plate lithosphere [*Rapanui Scientific Party et al.*, 1988; *Martinez et al.*, 1991; *Naar and Hey*, 1991; *Naar et al.*, 1991; *Hekinian et al.*, 1996]. Extension ahead of the propagating rift tip causes faulting of preexisting crust, creating a deep region within the rift valley known as the Pito Deep, with >4000 m of relief along its walls and a maximum depth to the valley floor of ~6000 m below sea level. The southwest facing scarps, which bound the northern side of the PDR and delineate the southern edge of the Nazca plate, cut across the local abyssal hill fabric, forming a natural cross section of Nazca plate crust.

[6] Previous geophysical studies of the PDR region include bathymetric (SeaBeam), side-scan sonar (SeaMarc II and GLORIA), magnetic, and gravity surveys [*Rapanui Scientific Party et al.*, 1988; *Searle et al.*, 1989; *Martinez et al.*, 1991; *Naar and Hey*, 1991]. These data show that the north wall of the PDR consists of northwest-southeast trending, structurally unified blocks of crust that extend for tens of kilometers along strike and <20 km across strike [*Rapanui Scientific Party et al.*, 1988; *Martinez et al.*, 1991; *Naar and Hey*, 1991; *Naar et al.*, 1991]. The southwest faces of these blocks form the northern walls of the PDR, which are steep (>20°) with good exposures of outcrop. The northeast facing slopes are shallower and sedimented, with abyssal hill fabric similar to the Nazca plate [*Rapanui Scientific Party et al.*, 1988; *Martinez et al.*, 1991; *Naar et al.*, 1991]. Plate reconstructions based on abyssal hill lineament patterns and magnetic anomalies suggest that the northwest-southeast trending walls of the PDR are down-dropped and back-tilted blocks of Nazca plate crust that were faulted <1 Ma ago by the slow (~10 mm/a), northwesterly propagation of the East Rift [*Rapanui Scientific Party et al.*, 1988; *Naar and Hey*, 1991; *Naar et al.*, 1991]. Magnetic anomaly 2A, which can be extrapolated across the

PDR from the Nazca plate to the north, suggests that the exposed Nazca crust was generated ~3 Ma ago near 23°S (just north of the East Pacific Rise (EPR)–Easter junction) along the fastest spreading portion of the SEPR [*Martinez et al.*, 1991; *Naar et al.*, 1991].

[7] To determine if the crustal sections exposed in the PDR are truly representative of SEPR crust, it is necessary to examine how the Easter Microplate influences spreading along the SEPR near 23°S. In the present tectonic configuration, Nazca crust formed between 22°S and 23°S becomes part of a broad wedge-shaped region of deformation north of the Pito Fracture Zone [*Naar and Hey*, 1989; *Rusby and Searle*, 1993]. Side-scan sonar and magnetic data show that the local northeast-southwest abyssal hill fabric has been rotated about a vertical axis in the clockwise direction [*Searle et al.*, 1989; *Zukin and Francheteau*, 1990; *Rusby and Searle*, 1995; *Varga et al.*, 2008] but that the internal architecture of the back-tilted fault blocks that bound the PDR has been little disturbed by the opening of the PDR or by deformation in the northern transform wedge [*Rapanui Scientific Party et al.*, 1988; *Hey et al.*, 1985; *Naar et al.*, 1991; *Cogne et al.*, 1995]. Thus, while the current configuration of the PDR is a product of extension ahead of a spreading center slowly propagating through deformed Nazca crust, the northern walls of the PDR expose a largely undisturbed natural cross section of ~3 Ma old EPR lithosphere.

[8] Whether the PDR crustal sections are typical of crust formed at superfast spreading rates is less clear. Today, the SEPR spreading rate decreases southward from ~160 mm/a near 22°S [*Naar and Hey*, 1989; *Rusby and Searle*, 1995] to ~140 mm/a near the SEPR-Easter intersection (~23°S [*Naar and Hey*, 1989, 1991]). The southward decrease in spreading rate is correlated with an increase in axial depth and in the MgO content of axial glasses, indicating a decreasing extent of fractionation toward the EPR-Easter intersection [*Sinton et al.*, 1991]. On the basis of these trends, *Sinton et al.* [1991] suggested that this portion of the SEPR is starting to fail, similar to the failing rift at the SEPR overlapping spreading center at 20.7°S. The timing of rift propagation must be considered, however, to understand the influence of a failing rift on the SEPR at the time the PDR crustal sections were formed (~3 Ma).

[9] Plate reconstructions based on magnetic patterns and other geophysical data differ on the timing for the onset of rift propagation [*Handschumacher et al.*, 1981; *Naar and Hey*, 1991; *Rusby and Searle*, 1995] but agree that the tip of the East Rift was located south of 24°S at ~3 Ma, reaching its present location (~23°S) only within the last ~2.5 Ma [*Naar and Hey*, 1991; *Rusby and Searle*, 1995]. During this time, the region of the SEPR that forms the western boundary of the Easter Microplate (known as the West Rift) began to fail by breaking into smaller segments and slowing. It is uncertain how much of the SEPR was affected by the failing ridge at this time, but since the East Rift had not yet reached its northerly location, it is reasonable to conclude that the effects of a failing rift were not as fully developed as they are today. Thus, we assume that the crust exposed in the northern walls of the PDR was accreted along a segment of the EPR spreading at rates of >140 mm/a, providing a rare "tectonic window" into superfast spreading oceanic crust.

[10] Three reconnaissance dives were conducted along two major escarpments on the northern wall of the PDR in 1993 using the manned submersible *Nautile* (Figure 2) [*Francheteau et al.*, 1994]. Observations from these dives described discontinuous exposures of lithologies similar to those identified in ophiolite complexes, which can be assembled into a nearly complete section of oceanic crust [*Moores and Vine*, 1971]. A northeast transect upslope on a scarp known as the "Jalapeno Ridge" (*Nautile* 09) revealed an upper basaltic volcanic unit exposed in the top ~350 m of the wall, consisting primarily of variably fractured pillow lavas. The volcanic unit is sparsely intruded by dolerite dikes and abruptly transitions downward into a sheeted dike complex that is >500 m thick before the bottom contact is obscured by talus. The dikes are locally sinuous, with orientations ranging from near vertical to moderately steeply dipping to the southeast, and are separated in some places by screens of brecciated material. An area of hydrothermal stock work was observed over a thickness of ~40 m within the sheeted dike unit [*Francheteau et al.*, 1994]. Observations during two deeper dives southeast of Jalapeno Ridge (*Nautile* 06 and 03) found similar exposures of basaltic lavas and sheeted dikes. In the upper ~400 m of crust, the volcanic unit crops out irregularly and contains a greater fraction of sheet and lobate lavas compared to the Jalapeno Ridge. A somewhat fractured sheeted dike complex, which is similar in thickness and appearance to the unit exposed on the Jalapeno Ridge, overlies outcrops consisting of both dolerite dikes and gabbro. Olivine gabbro was recovered from the deepest depths along the scarp (~5000 to 3800 m) and occurs in intermittent outcrops over ~250 m [*Francheteau et al.*, 1994; *Constantin et al.*, 1996; *Hekinian et al.*, 1996].

[11] We revisited the northern PDR escarpments in 2005 during a nested scale study that used the DSL-120 side-scan sonar, the *Jason II* ROV, and the *Alvin* human occupied vehicle (HOV) for low- to high-resolution mapping and sampling. The investigation focuses on areas previously examined by the 1993 *Nautile* dive program, which revealed excellent exposures of shallow level crust along the Jalapeno Ridge, hereinafter referred to as area A, and deeper level crustal units to the southeast, known as area B. The study areas are each ~5 km wide and are separated by ~14 km. Assuming a constant half spreading rate of 72 mm/a, each study area represents ~69 ka of spreading. Long transects by *Jason II* (9) and shorter transects by *Alvin* (12) cover depths from ~4000 m to ~2500 m upslope across both study areas. Dive spacing is commonly less than a kilometer, although some dive tracks intersect one another (Figure 2), allowing samples to be collected over small (meter) and large (hundreds of meters) spatial scales.

[12] Detailed observations from the multiple 2005 *Jason II* and *Alvin* dives to the northern PDR scarp reveal in greater detail the architecture of the ocean crust (Figure 3). Lithologies observed in the PDR were anticipated from the few 1993 *Nautile* dives: an upper unit of basaltic lavas, an underlying sheeted dike complex, and a lower unit of gabbroic rocks (Figures 3 and 4). The volcanic unit is dominated by pillow lavas with only sparse occurrences of sheet flows and lobate lavas, and varies in thickness from ~100–500 m. The underlying sheeted dike complex consists of dikes that are nearly vertical to steeply dipping

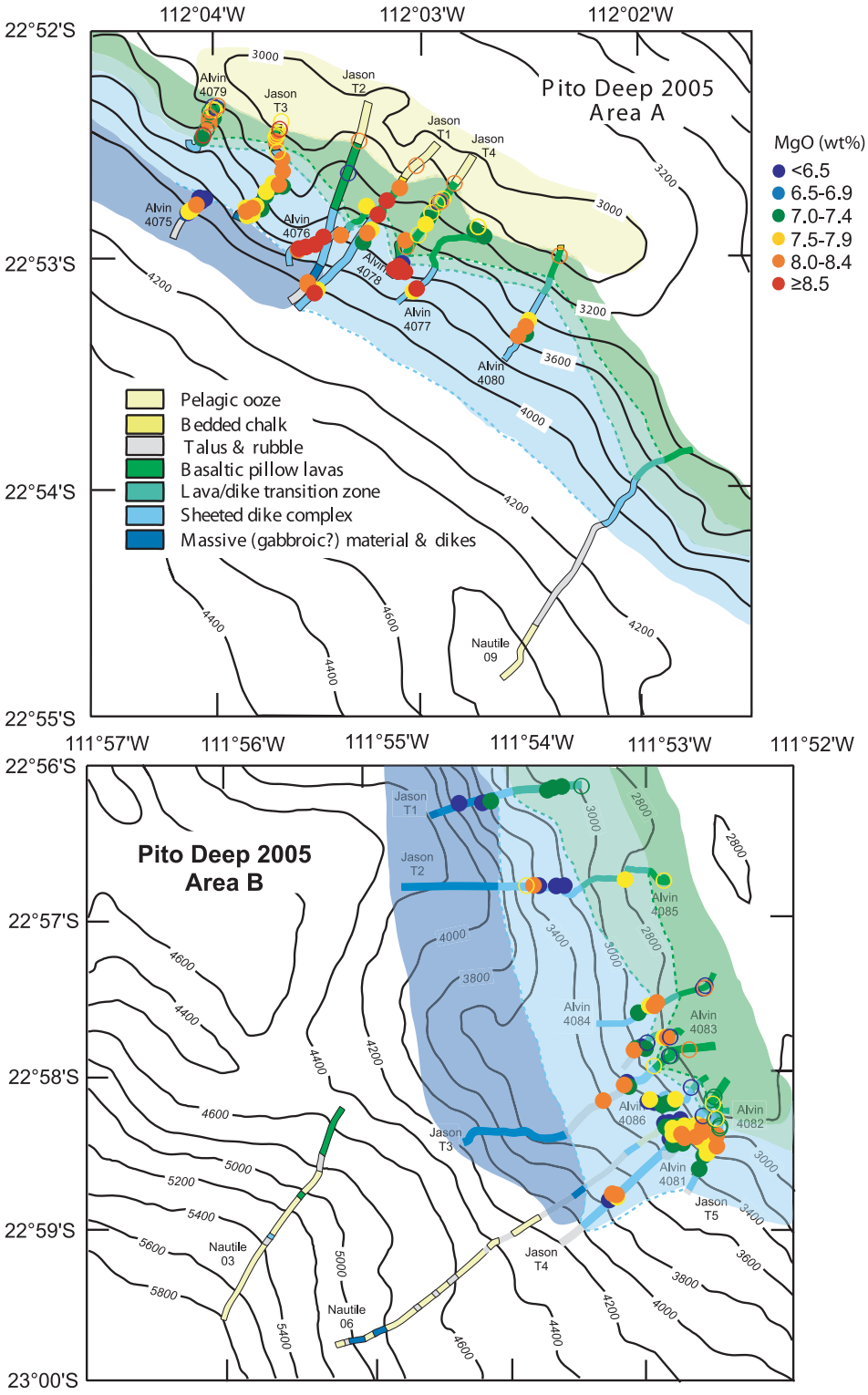

Figure 2. *Nautile* (1993), *Jason II* (2005), and *Alvin* (2005) dive tracks in study areas (top) A and (bottom) B showing observed lithologic units [*Karson et al.*, 2005]. In situ dikes (solid circles) and lavas (open circles) analyzed in this study are colored coded by MgO (wt %).

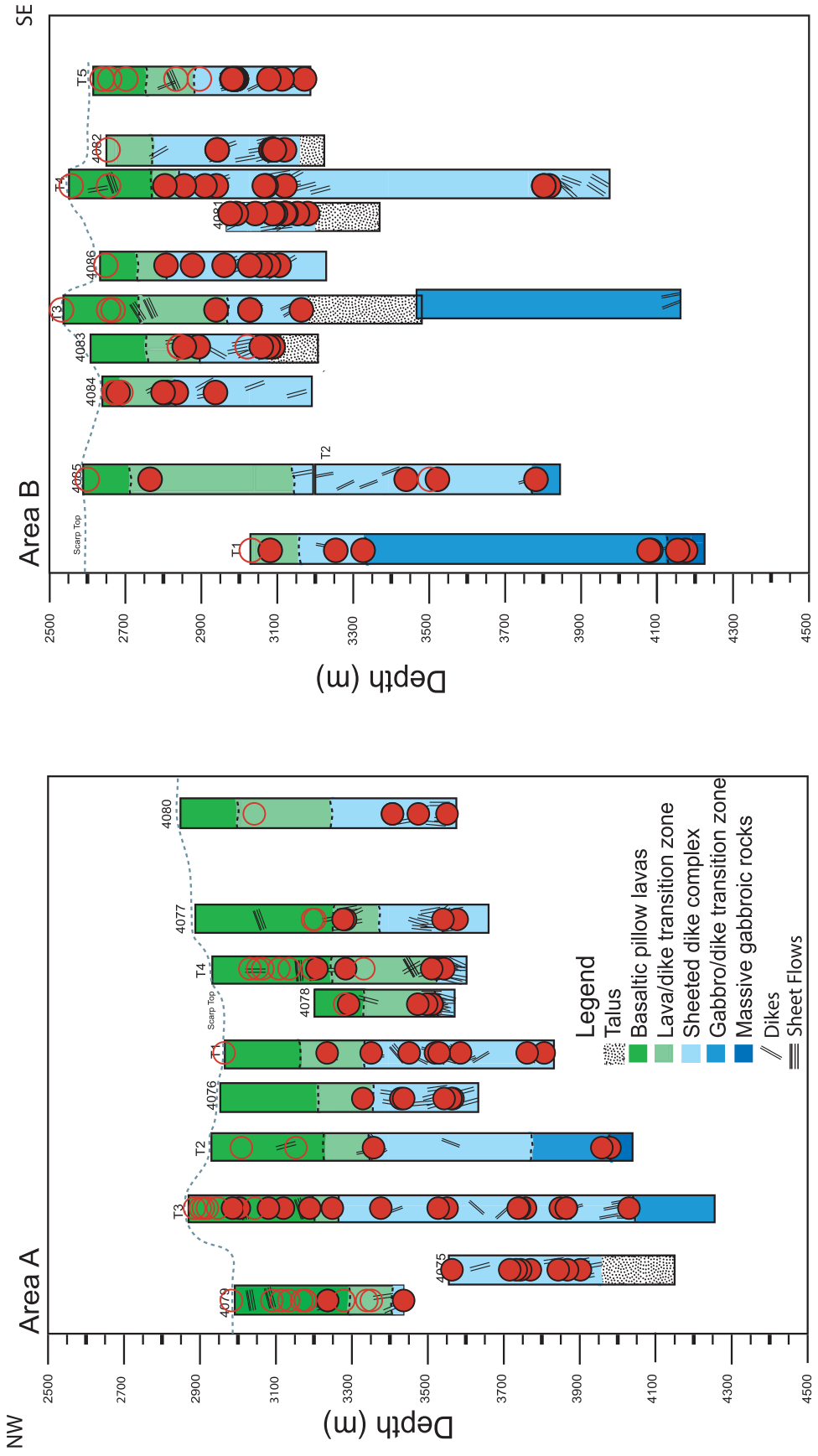

Figure 3. Lithologic columns for study areas A and B [*Morgan et al.*, 2005] showing locations of in situ dikes (solid circles) and lavas (open circles) analyzed in this study. Lithologic units are based on observations from each dive transect.

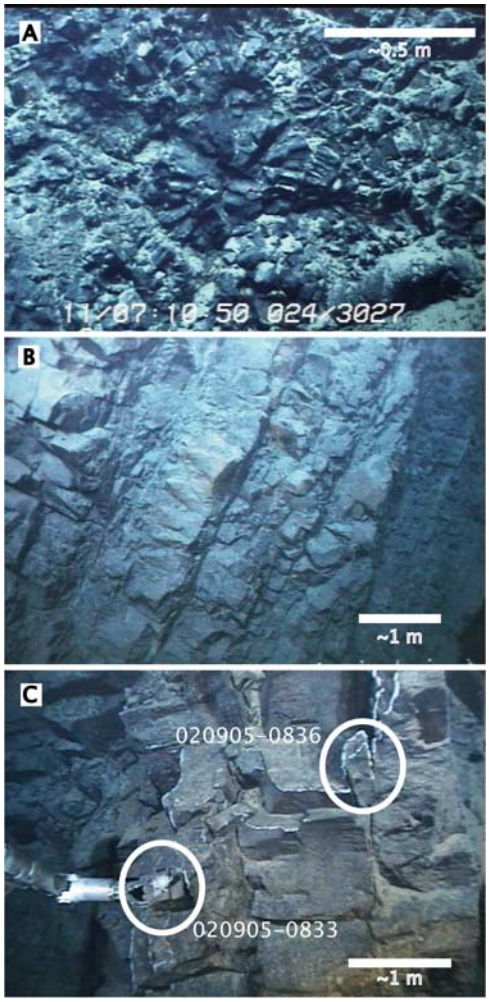

Figure 4. Photographs of lithologic units observed in area A. (a) Pillow lavas from *Jason* Transect 3, 3027 m depth. (b) Sheeted dikes from *Jason* Transect 1, 3504 m depth. (c) Closely spaced dikes 020905-0833 and 020905-0836 sampled from *Jason* Transect 3, 4009 m depth.

(65°–80°) to the southeast, and ranges in thickness from 700 to 1000 m. Outcrops of massive gabbroic rocks are exposed at the greatest depths (>4000 m), where the maximum thickness of the unit reaches ~700 m before the bottom contact is obscured by talus. Contacts between these units are transitional; dikes intrude lavas near the top of the sheeted dike complex and intrude gabbros near its base. On average, the transition zones are ~200 m thick. Overall, apparent deformation is low and mostly confined to local areas of brecciation, fault gouge, and hydrothermal veining.

3. Sampling and Sample Description

[13] Our 2005 *Alvin* and *Jason II* expedition to the northern wall of the PDR recovered an extensive suite of rock samples from the upper crust. More than 400 samples were collected in situ from outcrops of basaltic lavas (134), sheeted dikes (219), and massive gabbros (26), as well as fault breccias (32) and hydrothermally altered materials (10). Imaging and observations from the *Alvin* and *Jason II* dives provide excellent control on sample locations and field relationships, resulting in the fine-scale sampling of 11 pairs of dikes spaced less than one meter apart (Figure 4). An additional 28 pairs of dikes and 5 pairs of lavas were collected within 25 m of each other. In the context of oceanic studies, the PDR sample suite is unmatched in sampling detail and geologic control.

[14] This study focuses on samples recovered from the PDR lava unit and sheeted dike complex. The chemical compositions of gabbro and hydrothermally altered or brecciated material are reported and discussed elsewhere [*Hayman and Karson*, 2006; *Perk et al.*, 2007; *Heft et al.*, 2008]. Overall, dikes and lavas are similar in texture and are aphanitic to sparsely phyric. All lavas and most of the dikes are vitrophyric with a felty texture where fine-grained (<1 mm) plagioclase laths are set in an intergranular matrix of pyroxene and devitrified glass. Only 30% of dikes exhibit a medium (1–5 mm) grained doleritic texture. Most samples are aphyric, but a few samples of lavas are weakly porphyritic, containing fewer than 3% phenocrysts. In hand sample, visible phenocrysts are dominated by plagioclase laths of up to 2 mm in length.

[15] Most samples are altered to some degree, as indicated by veins of altered minerals (chlorite and clay) and greenish-brown alteration halos that line fractures and sample exteriors. The altered material, easily distinguished from the fresh, gray interiors, was avoided in the sample preparation procedure prior to chemical analysis. Of the nearly 350 samples that were collected from the sheeted dike complex and extrusive section, 205 were found to be suitable for chemical analyses. All of the dikes and lavas have <2.5 wt % loss on ignition (LOI), a measure well correlated with alteration [*Alt*, 1993]. Limiting the analyses to samples with LOI < 1.5 wt % reduces the number of suitable samples to 141. Examination of the variability of elements known to be susceptible to transport during low-temperature seawater interaction (e.g., Rb, Ba, Sr, and Cs [*Andrews*, 1977; *Humphris et al.*, 1980; *Alt*, 1993]) suggests that these elements may have been variably mobilized without visible signs of alteration; these elements are therefore excluded from further interpretation below.

4. Analytical Methods

[16] Major and trace element analyses were performed at Duke University on whole rock powders, which were prepared from the fresh crystalline interiors of dikes and lavas and crushed by hand using an agate mortar and pestle. Major element concentrations were measured by direct current plasma (DCP) emission spectrometry (Fisons SpecterSpan 7) following methods modified after *Klein et al.* [1991]. Si, Al, Ca, Fe, Mg, Na, Mn, and Ti were analyzed in a 1:4750 dilution while K, Ba, and P were analyzed in a 1:250 dilution. Concentrations of low-abundance trace elements (in a 1:10,000 dilution) were measured by inductively coupled plasma–mass spectroscopy (ICP-MS; VG PlasmaQuad 3) using a procedure modified after *Cheatham et al.* [1993]. Various standards, a blank, and a solution to monitor machine drift were also analyzed with each batch of samples run by DCP and ICP-MS. The standards used for calibration in both DCP and ICP-MS runs included the

Table 1. Major and Trace Element Compositions of Pito Deep Rift Dikes and Lavas[a]

	Sample								
	020705-1408	020805-0108	020905-1404	022305-0636	4077-1718	4079-1920	4084-1830	4085-1935	4086-2006
Study area	A	A	A	B	A	A	B	B	B
Jason Transect	1	1	3	5					
Morphology[b]	d	p	d	p	d	p	d	p	p
Lithologic zone[c]	D	V	D	T	D	V	T	V	V
Depth (m below sea level)	3657	3042	3676	2829	3538	3114	2768	2589	2664
Latitude (°S)	22.884	22.878	22.882	22.973	22.886	22.873	22.959	22.946	22.967
Longitude (°W)	112.056	112.051	112.063	111.875	112.051	112.067	111.882	111.882	111.877
SiO_2 (wt %)	51.8	50.6	50.9	50.8	49.2	51.7	52.4	52.1	50.9
TiO_2	1.44	1.53	1.51	1.83	1.16	1.70	1.43	1.42	1.93
Al_2O_3	13.9	14.9	13.9	13.8	15.2	14.3	14.4	14.6	13.5
Fe_2O_3*	11.9	10.9	12.9	13.5	10.0	9.7	9.4	9.3	12.0
MnO	0.22	0.18	0.20	0.22	0.17	0.20	0.20	0.20	0.21
MgO	7.27	8.21	7.65	7.25	9.16	7.31	7.87	7.52	6.78
CaO	10.5	11.8	10.9	10.5	11.1	11.7	12.4	12.3	10.9
Na_2O	2.75	2.60	3.12	2.86	2.49	2.70	2.57	2.55	2.71
K_2O	0.04	0.23	0.06	0.09	0.06	0.22	0.21	0.22	0.13
P_2O_5	0.16	0.42	0.50	0.36	0.26	0.40	0.30	0.29	0.43
Total	99.91	101.35	101.60	101.22	98.88	99.85	101.10	100.44	99.51
Low FeO* Group[d]						X	X	X	X
FeO*	10.7	9.8	11.6	12.2	9.0	8.7	8.4	8.3	10.8
Mg #	55.1	60.2	54.3	51.9	64.6	60.2	62.7	61.9	53.1
LOI	0.9	0.5	0.9	0.9	1.8	0.3	0.4	0.5	0.3
Sr (ppm)	78	147	99	95	89	135	126	112	113
Ba	2.59	16.95	128.58	1.66	1.72	21.29	14.27	11.33	10.22
Zn	75	87	47	104	48	91	90	83	110
Cu	74	64	142	67	12	78	67	73	62
Ni	61	117	113	47	98	60	80	93	51
V	250	314	352	382	283	373	318	346	407
Sc	39.3	39.2	43.7	42.6	39.4	44.1	42.3	45.3	43.4
Cr	205	325	283	54	378	204	164	252	90
Y	29	34	27	41	28	45	36	38	48
Zr	48	114	102	116	58	121	88	84	128
Be	0.34	0.66	1.09	0.50	0.73	0.28	0.44	0.45	0.61
Co	44.1	41.4	43.4	42.6	41.6	46.2	48.3	49.3	43.0
Rb		1.74	10.12		0.15	1.12	0.56	0.36	1.03
Nb	0.60	4.29	19.52	1.32	0.91	2.31	1.39	1.33	2.07
Cs	0.003	0.021	0.096		0.006	0.023	0.013	0.014	0.016
La	1.29	4.51	14.53	2.71	1.93	3.65	2.45	2.42	3.43
Ce	4.99	13.54	37.15	10.05	7.34	12.45	8.42	8.71	11.96
Pr	1.00	2.20	5.38	1.90	1.39	2.24	1.56	1.56	2.23
Nd	6.08	11.19	24.35	10.53	7.69	11.67	8.78	9.04	12.36
Sm	2.68	3.65	6.01	3.93	2.81	4.12	3.21	3.19	4.66
Eu	1.03	1.26	2.02	1.19	1.02	1.42	1.17	1.12	1.52
Gd	4.23	4.76	6.26	5.42	3.84	5.61	4.79	4.08	6.49
Tb	0.78	0.87	0.98	0.85	0.73	1.08	0.87	0.74	1.14
Dy	5.26	5.76	5.29	6.99	4.83	7.30	5.90	5.91	7.98
Ho	1.08	1.23	0.99	1.56	1.03	1.57	1.28	1.29	1.77
Er	2.89	3.42	2.49	3.97	2.76	4.38	3.60	3.16	4.82
Yb	2.74	3.43	1.99	4.05	2.67	4.40	3.58	3.70	4.75
Lu	0.42	0.53	0.29	0.64	0.41	0.71	0.57	0.61	0.76
Hf	1.77	2.90	4.66	2.97	1.34	3.20	2.30	2.48	3.55
Ta	0.06	0.29	1.26	0.12	0.07	0.17	0.11	0.12	0.17
Pb	0.195	0.592	2.150	0.518	0.211	0.718	0.352	0.421	0.855
Th	0.045	0.272	1.196	0.078	0.043	0.142	0.079	0.097	0.114
U	0.019	0.110	0.403	0.034	0.014	0.084	0.150	0.042	1.622
Y/Nb	48	8	1	31	31	20	26	29	23
Nb/Ta	10	15	16	11	13	14	13	11	12
$(Ce/Yb)_N$	0.51	1.10	5.18	0.69	0.76	0.79	0.65	0.65	0.70
$(La/Sm)_N$	0.31	0.80	1.56	0.44	0.44	0.57	0.49	0.49	0.48

following: NBS-688, AII92-29-1 (a Mid-Atlantic Ridge standard), K1919 (a sample from the same lava flow as USGS BHVO-1), and U.S. Geological Survey standards BHVO-1, W2-1, BIR-1, and DNC. Samples solutions were run in duplicate and sometimes triplicate. In addition, multiple solutions were prepared for some samples and analyzed in separate runs. Reported uncertainty was determined by repeat analyses (~30) of standards as unknowns. Reproducibility for DCP analyses is 1–2% for all elements with the exception of< 5% for K. For ICP-MS analyses, reproducibility is 1–3% for rare earth elements (REE) and 1–4% for all other elements except Cs (<5%) and U (<5%).

[17] Lead isotope analyses were performed on 300–500 mg of whole-rock powder. Samples were dissolved in HF and HNO_3, converted to chlorides, then bromides. Isolation of Pb was accomplished using HBr anion exchange chemistry following the method of *Parrish et al.* [1987]. Isotope analyses were performed on a VG-SECTOR 54 mass spectrometer at the University of North Carolina at Chapel Hill in static multicollector mode with $^{208}Pb = 1–2 \times 10^{-11}$ A.

5. Results

5.1. Comparison to Variability in Global and EPR Basalt Compositions

[18] Representative major and trace element compositions of dikes and lavas from the PDR are presented in Table 1. All PDR data are compared, in Figure 5, to normal mid-ocean ridge basalts (NMORB) from the southern EPR, Kolbeinsey Ridge, and Mid-Cayman Rise, representing much of the global range in major element compositions. As a whole, PDR lavas range from relatively unfractionated to more evolved (Mg #s = 66 to 42; MgO = 9.3–5.9 wt %). Data from areas A and B generally overlap with glass and whole-rock compositions of lavas collected from 21°S to 23°S on the SEPR, the approximate latitude of the EPR where the PDR dikes and lavas were generated, with some clustering toward the upper and lower limits of FeO* and Al_2O_3, respectively. Like the SEPR lavas, PDR lavas are intermediate in major element composition compared to data from the Kolbeinsey Ridge and the Mid-Cayman Rise, which respectively represent lavas generated by large and small extents (and pressures) of melting [e.g., *Klein and Langmuir*, 1987].

5.2. Crystallization

[19] Overall, the PDR major element data show variations with MgO that are consistent with the effects of crystallization of a tholeiitic magma, specifically, increasing abundances of incompatible elements (e.g., FeO*, TiO_2, La, Nb, Zr) and decreasing abundances of compatible elements (e.g., Al_2O_3, CaO, and Ni) with decreasing MgO concentrations (Figures 5 and 6 and Table 1). Data from area A extend to more MgO-rich compositions compared to area B (Figure 5). Most of the more evolved (Mg # < 51) samples were recovered from area B and can be classified as FeTi basalts (FeO* > 12% and TiO2 > 2% [*Byerly*, 1980]). A group of samples, dominated by lavas, is offset from the main composition trend toward lower abundances of FeO* and somewhat elevated abundances of CaO and Al_2O_3 (Figure 5). A similar chemical distinction has been observed at the Hess Deep Rift [*Stewart et al.*, 2003] and has been interpreted as the result of the accumulation of plagioclase. The petrogenesis of the low FeO* group, and the implications for magma eruptability, are explored in a separate study [*Pollock*, 2007].

[20] The MELTS program (version 5.0.0 [*Ghiorso and Sack*, 1995; *Asimow and Ghiorso*, 1998]) was used to model liquid lines of descent (LLDs) at 0.5-, 1-, and 3-kbar pressure (Figure 5). Trace element LLDs (Figure 6) were calculated assuming perfect fractional crystallization using mineral assemblages from the MELTS model and partition coefficients (K_d) from *Bedard* [1994]. The composition of a relatively unevolved (Mg # 65; MgO 9.3 wt %) PDR sample (4077–1718) was used as the parental magma composition for calculation of LLDs for both anhydrous melt and melt with 0.3 wt % H_2O at a range of pressures. The models produce typical tholeiitic differentiation trends through the successive fractional crystallization of olivine, plagioclase, clinopyroxene, and spinel. The PDR major and trace element data are best described by up to 63% crystallization along calculated anhydrous LLDs up to 1 kbar of pressure. Olivine appears first in the crystallizing assemblage and is joined by plagioclase at 8.7 wt % MgO after only ~5% total crystallization. CaO concentrations initially increase in the liquid during crystallization but start to decrease with the appearance of clinopyroxene on the liquidus at 8.3 wt % MgO (after 17% crystallization). Clinopyroxene, olivine and plagioclase fractionate together until a Mg-rich spinel starts to crystallize at 7.4 wt % MgO (38% total crystallization). After ~40% crystallization, when the evolved FeTi basalts begin to form, the fractionating assemblage consists of a minor portion of Ti-rich spinel (titanomagnetite) and approximately equal fractions of clinopyroxene and plagioclase.

[21] For both major and trace elements, data from area B generally follow the LLD while area A compositions are more widely scattered (Figures 5 and 6). Some samples, however, are offset from the anhydrous 1-kbar LLD toward lower FeO*. Small amounts of water have been shown to

[1] Auxiliary materials are available at ftp://ftp.agu.org/apend/jb/2007jb005436.

Notes to Table 1:

[a] Major and trace element data for representative whole rock samples from the Pito Deep Rift. Complete data sets are available as in the auxiliary material.[1] Major element oxides are reported in wt %; trace elements are reported in ppm. Fe_2O_3* is total Fe as Fe_2O_3. FeO* is total Fe recalculated as FeO. Mg # is calculated as cation mol % [Mg/[Mg + Fe]] using the recalculated values for MgO and FeO*. LOI was measured by igniting each sample for 30 min at 950°C. Major elements and Sr, Sc, Zn, and V were analyzed by DCP. Reproducibility for DCP analyses is 1–2% for all major and minor elements with the exception of K (<5%). The remaining trace elements were analyzed by ICP-MS, for which the reproducibility is 1–3% for REE and 1–4% for all other elements except Cs (<5%) and U (<5%). Replicate analyses of standards are in agreement with previously published values (see auxiliary material of *Stewart et al.* [2002]).

[b] Morphology refers to dike (d), pillow (p), massive (m), sheet flow (s), or talus (t).

[c] Lithologic zone refers to dike unit (D), volcanic unit (V), dike-lava transition zone (T), and gabbro-dike transition zone (GDT).

[d] Samples that fall into the low FeO* Group are indicated by X.

suppress the onset of plagioclase crystallization [e.g., *Green and Ringwood*, 1968; *Sinton and Fryer*, 1987; *Sisson and Grove*, 1993; *Danyushevsky*, 2001], leading to suppressed iron enrichment. An LLD calculated for the parental magma composition with 0.3 wt % H_2O came closer to reproducing the low FeO* of this sample group but provides a poor fit in terms of other major elements (e.g., Al_2O_3), suggesting that the low FeO* samples cannot be attributed to a reasonably hydrous parent magma.

[22] Trends observed in chondrite-normalized REE data [*Sun and McDonough*, 1989] are also consistent with the effects of fractional crystallization (Figure 7). Evolved samples, with lower Mg #s, generally show higher REE abundances and more negative Eu anomalies compared to less evolved, higher Mg # samples. Thus, to first-order, low-pressure fractional crystallization accounts for much of the variation observed in the major and trace element data. However, there is diversity among the PDR samples, particularly evidenced by variations in the concentrations of trace elements and their ratios at constant MgO values, that cannot be accounted for by fractional crystallization. This dispersion suggests that, in addition to crystallization, factors related to source composition, mantle melting, and/or mixing conditions may affect the PDR suite.

5.3. Mantle Melting and Source Characteristics

[23] On the basis of chondrite normalized trace element and REE patterns, most of the PDR samples can be classified as normal MORB (NMORB) (Figure 7) [*Sun and McDonough*, 1989]. The majority of samples are depleted in highly incompatible elements ($(La/Sm)_N$ of 0.50 ± 0.05) with ratios of moderately incompatible elements near unity ($(Sm/Yb)_N$ of 1.13 ± 0.09). Exceptions are six samples from area A: one enriched MORB (EMORB, 020905–1404, $(La/Sm)_N$ of 1.56); one sample more depleted in the light REEs (LREEs) (020705–1408, $(La/Sm)_N$ of 0.31); and four MORB with flatter LREE patterns ($(La/Sm)_N$ of 0.83 ± 0.04). The latter samples are classified as transitional MORB (TMORB) on the basis of $(La/Sm)_N$ ratios, distinct Pb isotopic compositions (see section 5.4), and $K_2O > 0.15$ with $K_2O/TiO_2 \geq 0.12$ [*Bergmanis et al.*, 2007]. Only one of the transitional samples (4075–1912) has a K_2O/TiO_2 value (0.08) similar to NMORB (0.05 ± 0.03), but is classified here as a TMORB based on $(La/Sm)_N$ and Pb isotopes.

[24] Ratios of strongly and moderately incompatible trace elements (e.g., $(La/Sm)_N$, $(Ce/Yb)_N$, Y/Nb), which remain relatively constant over a reasonable extent of crystallization (<70% [*Gast*, 1968]), can be used to distinguish variations in the composition of the mantle source or melting conditions. The variability in $(La/Sm)_N$ and other

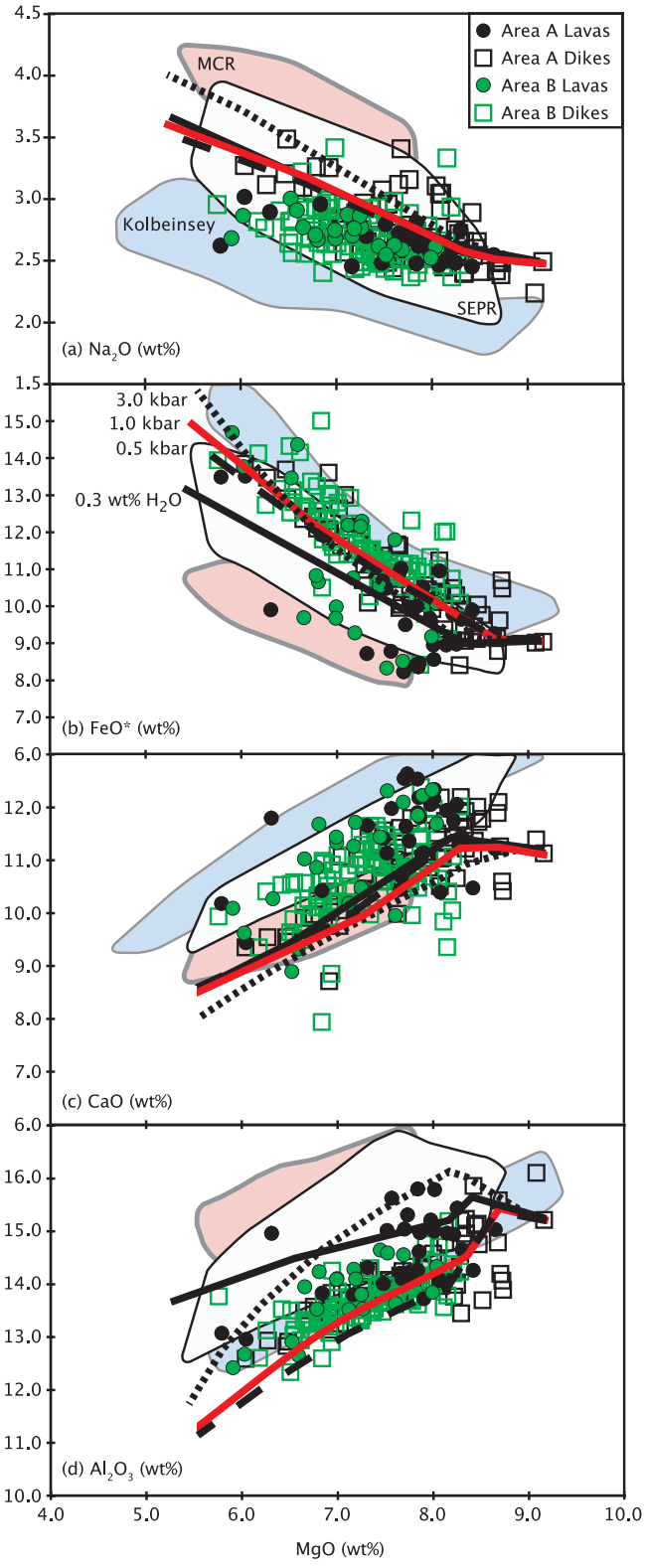

Figure 5. Major element variations for PDR Samples from area A (black) and area B (green) dikes (open squares) and lavas (solid circles). Symbols are larger than analytical error (±1 sigma). Fields show range in NMORB compositions of glasses and whole rocks from 21°S to 23°S on the EPR (white), Kolbeinsey Ridge (blue), and Mid-Cayman Rise (pink). Data for the fields are from the Ridge Petrological Database of the Ocean Floor (http://www.petdb.org). Oxide values plotted for each data set have been recalculated after converting Fe to FeO*. Liquid lines of descent (LLDs) are calculated using the MELTS program for 0.5-kbar (dashed), 1-kbar (red), and 3-kbar (dotted) anhydrous fractional crystallization. LLD for hydrated fractional crystallization (black) was calculated for a parent melt containing 0.3 wt % H_2O. Primary sample 4077-1718 (MgO 9.3 wt %) is used as a parental melt for all LLDs.

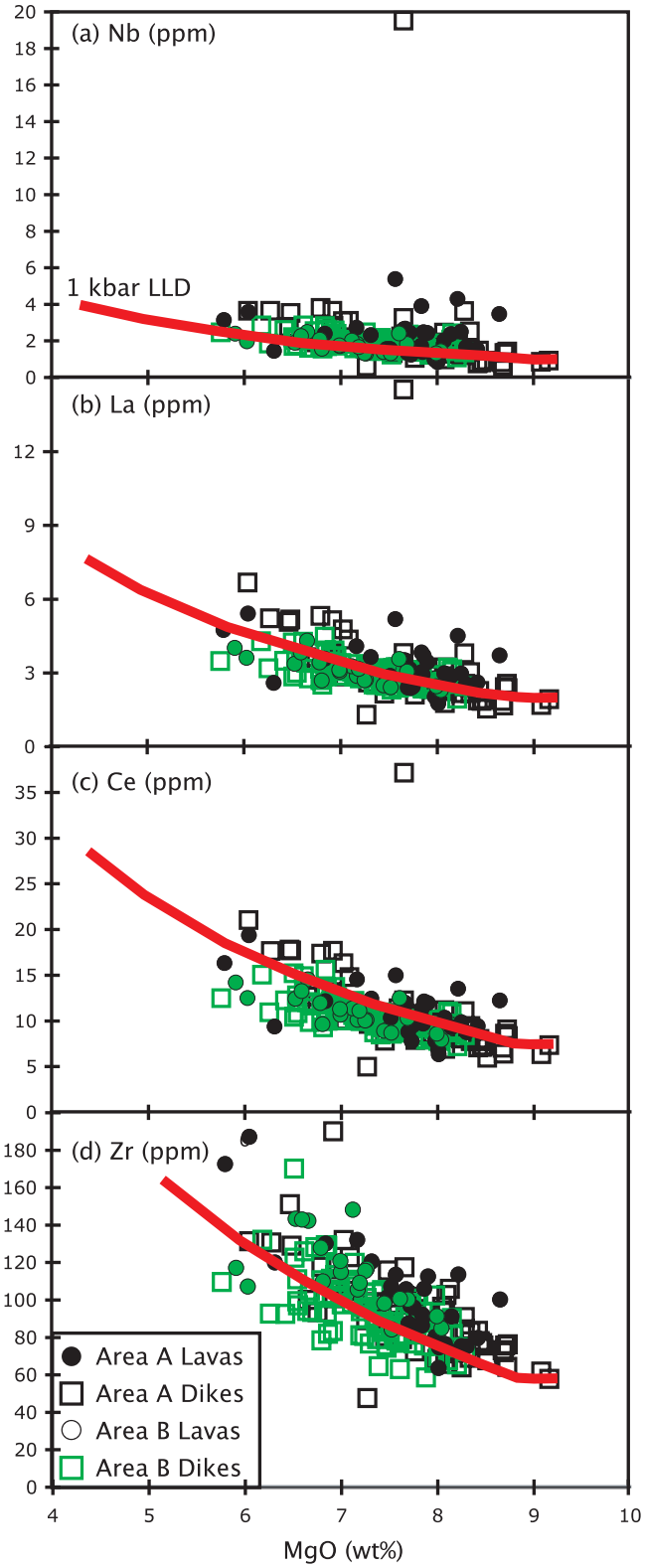

Figure 6. Variations in (a) Nb, (b) La, (c) Ce, and (d) Zr (ppm) with MgO (wt %) for area A (black) and B (green) dikes (open squares) and lavas (solid circles). The 1-kbar LLD (red) is calculated assuming fractional crystallization using partition coefficients from *Bedard* [1994].

incompatible trace element ratios is displayed in Figure 8. The PDR suite encompasses an expansive field that extends beyond the range of ratios that can be generated through crystal fractionation. Overall, trace element ratios from area B are relatively constant (e.g., $(La/Sm)_N$ 0.42–0.69) with MgO, but area A shows a considerably wider range of compositions (e.g., $(La/Sm)_N$ 0.31–1.56; Figure 8). Such diversity in the PDR trace element compositions suggests that either variations in melting a homogeneous mantle generated melts with a wide range of trace element ratios or that the PDR magmas were produced by mixing of melts from a heterogeneous mantle source.

[25] To determine the effects of source composition, ratios of strongly and moderately incompatible elements (Figure 8) were used to calculate curves for variable extents of melting of an enriched and a depleted mantle. Trace element compositions of depleted and enriched MORB mantle (DMM), modified after those reported by *Workman and Hart* [2005], were used as starting compositions. The enriched (EDMM) and depleted (DDMM) mantle sources were defined by *Workman and Hart* [2005] based on Sr-Nd-Pb isotopes. To provide a more accurate approximation of the depleted mantle composition for the PDR data, the DDMM composition was modified to be slightly more depleted in La (0.103 ppm) and Nb (0.0695 ppm), and slightly more enriched in Zr (4.465 ppm).

[26] Overall, the PDR data form curved trends that are best approximated by mixing of melts from a heterogeneous mantle. In particular, the highly variable data from area A require melting of enriched and depleted mantle sources to generate the range in trace element ratios between the enriched MORB (EMORB) and LREE-depleted sample. Area B samples show more limited variability in trace element ratios and can be generated through various degrees of melting of the depleted mantle component (DDMM) alone. However, the lack of EMORB sampled from dikes and lavas in area B does not preclude a heterogeneous mantle as a realistic explanation for the source composition of the PDR data set. Compositional variations in gabbros recovered from the deeper sections of area B suggest the presence of an LREE enriched magma [*Perk et al.*, 2007]. In fact, patterns in Pb isotope compositions, including those of area B, reveal that the PDR samples were generated from a heterogeneous mantle with two isotopically distinct enriched components.

5.4. Pb Isotopes: A Three-Component SEPR Mantle

[27] Figure 9 and Table 2 present Pb isotope compositions for PDR samples that were previously determined by REE patterns to be LREE-depleted (020705–1408), normal MORB (NMORB; 13 samples), transitional MORB (TMORB; 4 samples), and enriched MORB (EMORB, 020905–1404). The PDR Pb isotope ratios (ranging 18.308–18.764 in $^{206}Pb/^{204}Pb$; 15.481–15.777 in $^{207}Pb/^{204}Pb$; and 37.722–38.158 in $^{208}Pb/^{204}Pb$) form an array that largely overlaps Pb isotopic compositions of seamount and axial lavas from the SEPR [*Sinton et al.*, 1991; *Bach et al.*, 1994; *Mahoney et al.*, 1994; *Niu et al.*, 1996; *Hall et al.*, 2006; *Bergmanis et al.*, 2007], but extends to more radiogenic values of $^{207}Pb/^{204}Pb$ and $^{208}Pb/^{204}Pb$ (Figure 9). Variability in the PDR Pb isotope data is weakly correlated with REE patterns. For example, PDR TMORB

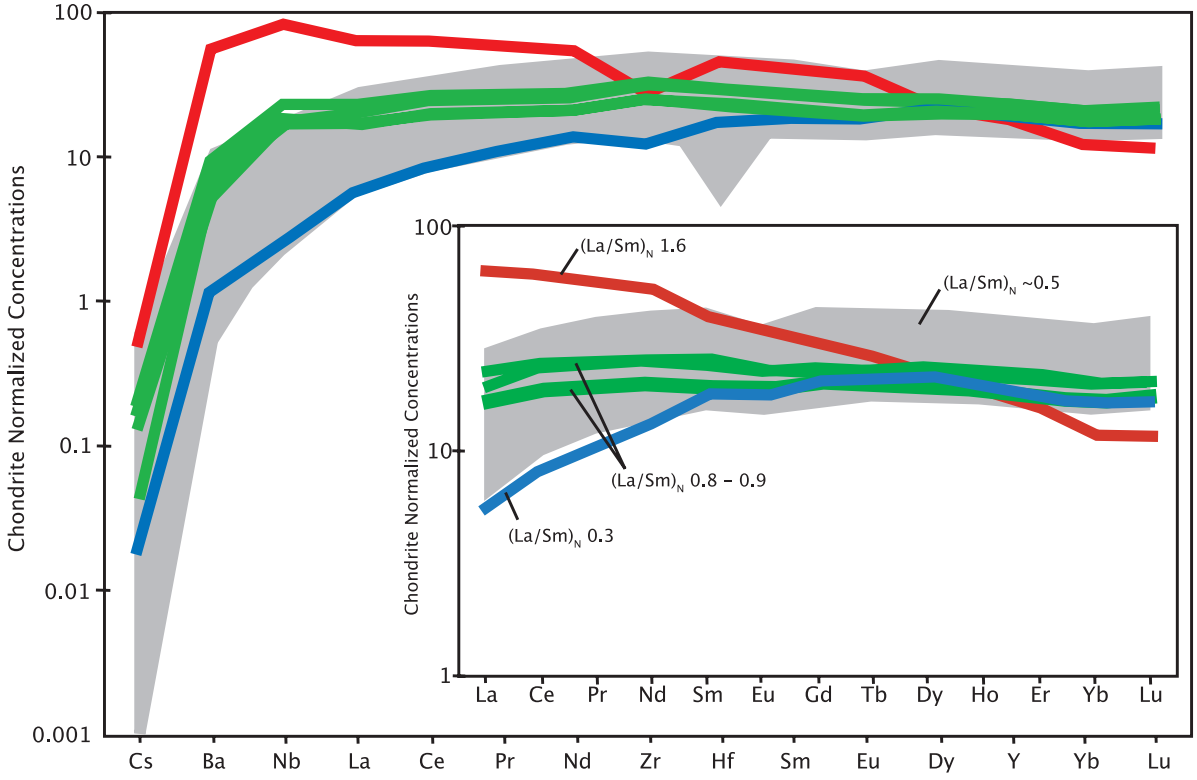

Figure 7. Chondrite-normalized trace elements abundances [*Sun and McDonough*, 1989] in order of increasing compatibility. Inset shows chondrite-normalized rare earth elements (REE). Most of the PDR sample are incompatible element depleted NMORB (gray fields; $(La/Sm)_N \sim 0.5$). One sample shows more depleted LREE (blue; $(La/Sm)_N$ 0.3). Four samples can be classified as TMORB (green; $(La/Sm)_N$ 0.8–0.9) and one as EMORB (red; $(La/Sm)_N$ 1.6). All enriched, transitional, and depleted samples are from area A.

and some NMORB fall along the more and less radiogenic portions of the SEPR field, respectively. At a given value of $^{206}Pb/^{204}Pb$, however, the PDR EMORB, most NMORB, and the LREE depleted sample are offset from the SEPR field toward higher values of $^{207}Pb/^{204}Pb$ and $^{208}Pb/^{204}Pb$.

[28] Linear trends in Sr-Nd-Pb isotope data from the SEPR have been interpreted as mixing lines between enriched and depleted mantle sources [*Niu et al.*, 1996; *Hall et al.*, 2006; *Bergmanis et al.*, 2007]. The PDR data generally fall along these linear mixing trends (Figure 9), consistent with patterns in PDR trace element ratios that suggest mixing of melts from a heterogeneous mantle. Although a direct comparison to SEPR data is difficult because only Pb isotopes have been analyzed for the PDR suite, the PDR TMORB and NMORB that directly overlap the linear SEPR Pb isotopic arrays suggest that these samples were derived from a heterogeneous source similar to that underlying the present-day SEPR axis. Two compositional end-members have been previously defined for the SEPR mantle: an ambient NMORB source mantle with low $^{206}Pb/^{204}Pb$ and an incompatible element-enriched mantle component with higher $^{206}Pb/^{204}Pb$ [*Mahoney et al.*, 1994; *Hall et al.*, 2006; *Bergmanis et al.*, 2007]. Thus, PDR TMORB, which are more radiogenic than PDR NMORB, represent mixtures of melts with a higher proportion of the enriched end-member while the PDR NMORB that overlap the less radiogenic portion of the SEPR field have a greater proportion of the ambient depleted mantle.

[29] Most of the PDR NMORB and the EMORB, however, are offset from the SEPR mixing trend toward higher values of $^{208}Pb/^{204}Pb$ (by ~0.1–0.2) and $^{207}Pb/^{204}Pb$ (by ~0.05–0.1). This is somewhat unusual for the SEPR, even when analytical errors are considered. Elevated $^{207}Pb/^{204}Pb$ ratios have been measured in lavas collected along the East and West Rifts of the Easter Microplate [*Hanan and Schilling*, 1989; *Haase*, 2002] and in axial lavas from the SEPR south of the overlapping spreading center (OSC at 20.7°S [*Mahoney et al.*, 1994]), a significant axial offset associated with a southward propagating rift [*Macdonald et al.*, 1988]. These data form a linear array distinct from the SEPR trend in $^{207}Pb/^{204}Pb$ versus $^{206}Pb/^{204}Pb$ space (Figure 9) that has been attributed to mixing between a depleted MORB source and a plume-like mantle component similar to that present under Sala y Gomez [*Hanan and Schilling*, 1989; *Mahoney et al.*, 1994]. A similar explanation can be applied to the PDR EMORB and NMORB, but the nature of the inferred enriched component is somewhat different. Unlike the Sala y Gomez plume, the elevated $^{208}Pb/^{204}Pb$ and $^{207}Pb/^{204}Pb$ values of the PDR samples require an enriched component similar to EMII. Thus, the entire PDR Pb isotope data set can be explained by mixing of melts from a heterogeneous three-component mantle: a depleted mantle source, represented by SEPR NMORB; an enriched mantle source, represented by SEPR EMORB and PDR TMORB; and a more EMII-like mantle, with more radiogenic $^{207}Pb/^{204}Pb$ and $^{208}Pb/^{204}Pb$ values, represented

by PDR EMORB and most PDR NMORB. Mixing of melts between these dual enriched components and the depleted end-member produces mixing trends that are consistent with patterns in isotope and incompatible element ratios. Although PDR TMORB generally fall along the mixing line between EMORB and the LREE-depleted sample in incompatible element space, the Pb isotope data suggest that the TMORB are derived from a separate, third component of the mantle.

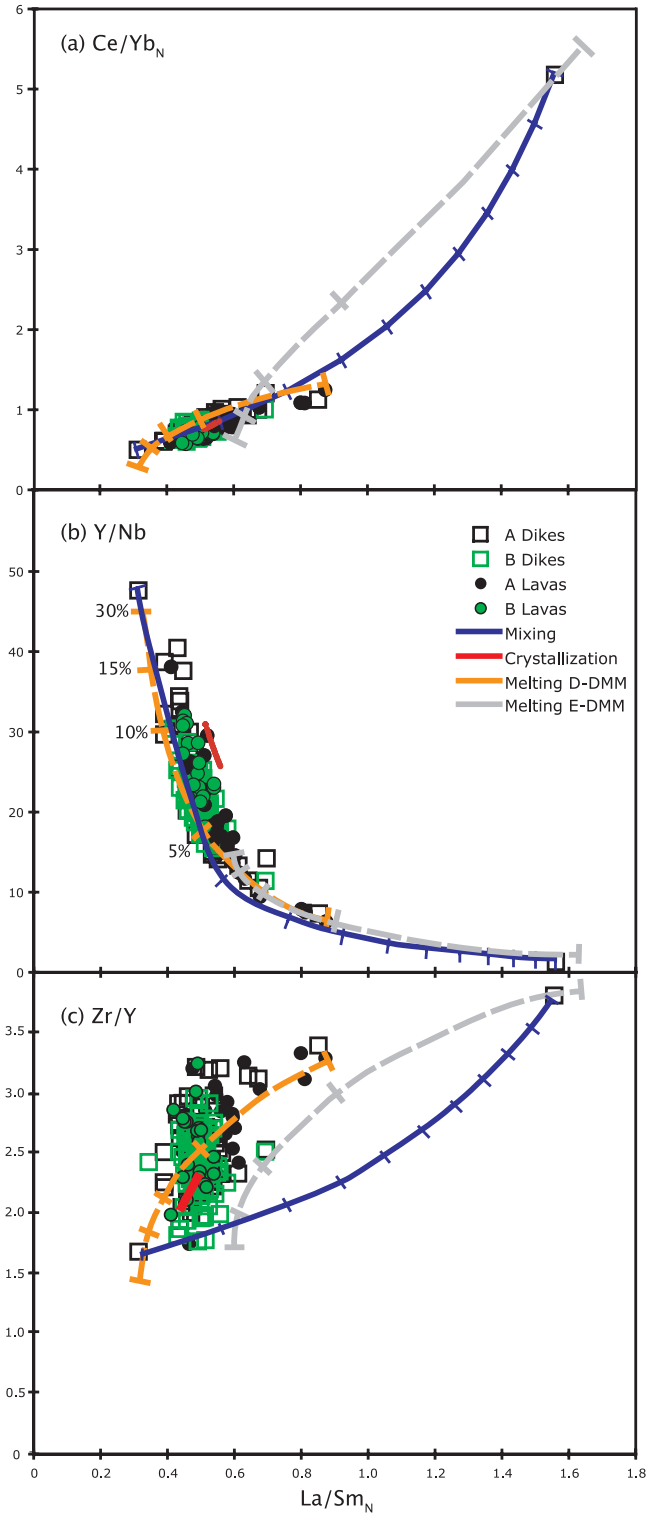

[30] It is interesting to note that the LREE-depleted PDR sample (020705–1408) does not fall along the least radiogenic portion of the mixing trends, as would be expected if it were derived from the depleted mantle end-member. Rather, the LREE-depleted sample is similar to most PDR NMORB, with more radiogenic $^{208}Pb/^{204}Pb$ and $^{207}Pb/^{204}Pb$ for its given value of $^{206}Pb/^{204}Pb$. Similarly, depleted MORB (DMORB) from the Siqueiros Transform have been reported to be more radiogenic in Pb compared to axial NMORB collected from 9°–10°N on the EPR [*Sims et al.*, 2002]. The decoupling between Pb isotope and incompatible trace element ratios suggests that the LREE-depleted sample represents a NMORB melt that was melted to a greater extent so as to become more depleted in incompatible elements but not less radiogenic in Pb. Trace element models support this interpretation, demonstrating that the LREE-depleted sample can be generated by a high degree of melting of the depleted MORB mantle (DDMM; Figure 8).

[31] The observation of a three-component mantle is significant in the context of the latitudinal variations in isotopes along the SEPR. The SEPR between 15.8°S and 20.7°S, well known as the Hump Region [*Cormier and Macdonald*, 1994], is characterized by a wide cross-axis area and a systematic along-axis trend in Sr-Nd-Pb isotope ratios that peaks at ~17.5°S [*Sinton et al.*, 1991; *Niu et al.*, 1996]. Pb isotopic compositions from the Hump Region are similar to those displayed by PDR TMORB, suggesting that the PDR TMORB were derived from a mantle source similar to that currently underlying the Hump Region. *Mahoney et al.* [1994] reported that the particular signature of mantle heterogeneity responsible for generating the elevated isotopic patterns in the Hump Region did not extend along the SEPR axis south of the OSC at 20.7°S, which was thought to have developed ~3 Ma [*Macdonald et al.*, 1988]. They propose a model in which a plume-like mantle composition is injected into the depleted mantle

Figure 8. Variations in trace element ratios (a) $(Ce/Yb)_N$, (b) Y/Nb, and (c) Zr/Y versus $(La/Sm)_N$ for dikes (open squares) and lavas (solid circles) from areas A (black) and B (green). Ratios of Ce/Yb and La/Sm are normalized to chrondrite values [*Sun and McDonough*, 1989]. Extent of variability caused by fractional crystallization (up to 65%) shown as a red line. Blue line shows mixing between the EMORB and LREE-depleted sample, marked at 10% increments. Gray dashed line indicates up to 30% incremental batch melting of EDMM [*Workman and Hart*, 2005], marked at 5, 10, and 15% melt intervals. In each increment, the mantle was melted to a small degree (1%) and pooled with melts from previous batches. Orange dashed line shows up to 30% incremental batch melting of *Workman and Hart*'s [2005] DDMM that has been modified to be more depleted in La (0.103 ppm) and Nb (0.0695 ppm) and more enriched in Zr (4.465 ppm). Bulk Ds from *Workman and Hart* [2005] for melting in the spinel stability field were used to generate the melting curves, with the exception of Ce and Yb (bulk Ds of 0.01 and 0.2, respectively) for melting of EDMM. Ce and Yb are slightly more compatible in the EDMM compared to the DDMM, though not compatible enough to require melting in the garnet stability field.

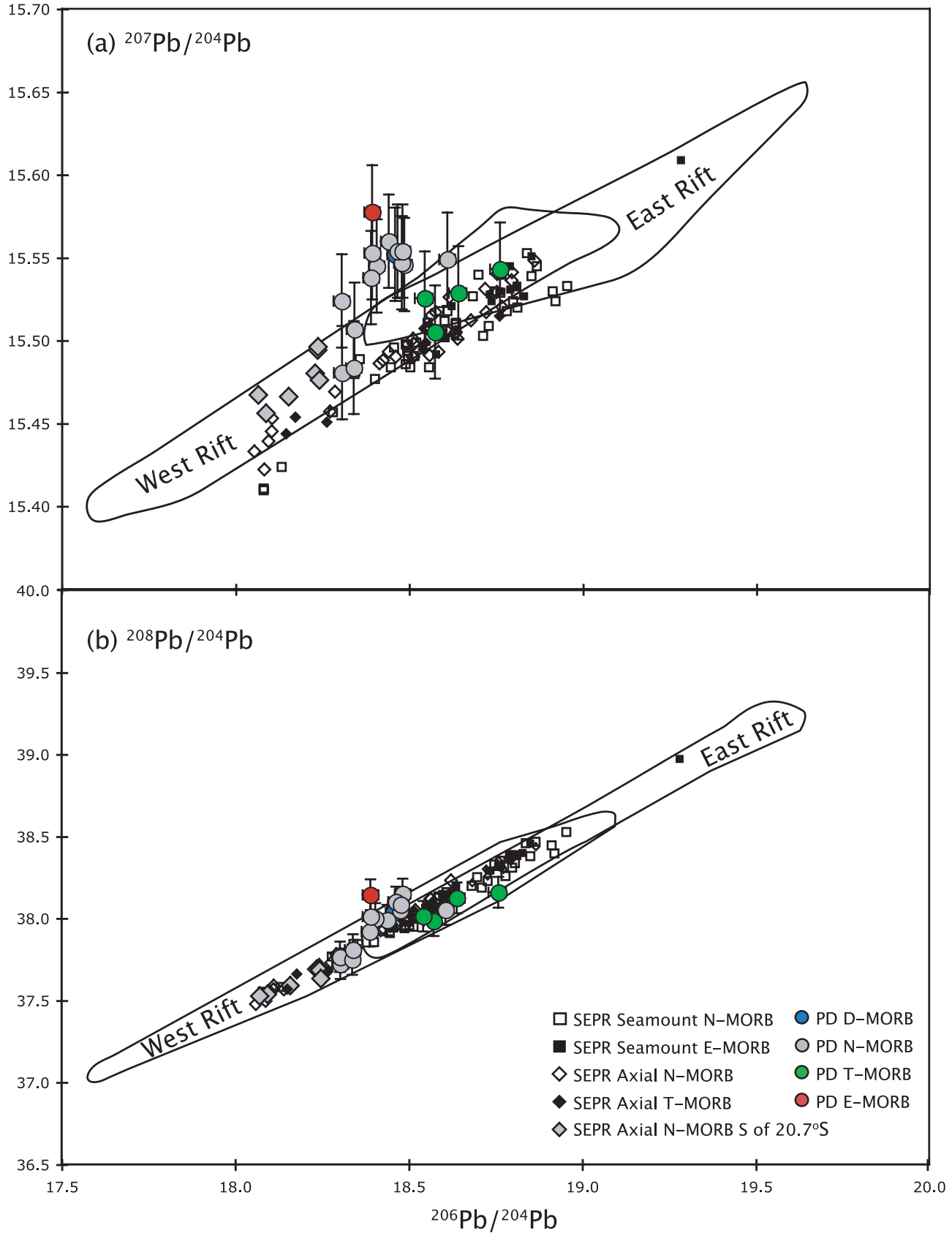
(a) 207Pb/204Pb
15.70
15.65
15.60
15.55
15.50
15.45
15.40
East Rift
West Rift
(b) 208Pb/204Pb
40.0
39.5
39.0
38.5
38.0
37.5
37.0
36.5
East Rift
West Rift
SEPR Seamount N-MORB
SEPR Seamount E-MORB
SEPR Axial N-MORB
SEPR Axial T-MORB
SEPR Axial N-MORB S of 20.7°S
PD D-MORB
PD N-MORB
PD T-MORB
PD E-MORB
17.5
18.0
18.5
19.0
19.5
20.0
206Pb/204Pb

Figure 9

Table 2. Lead Isotope Analyses for Selected PDR Samples[a]

Sample	$^{206}Pb/^{204}Pb$	$^{207}Pb/^{204}Pb$	$^{208}Pb/^{204}Pb$
020705-1408	18.462	15.552	38.034
020805-0108	18.764	15.543	38.158
020905-1404	18.396	15.577	38.143
021105-0627	18.577	15.505	37.984
021105-0639	18.645	15.529	38.124
021905-0148	18.308	15.524	37.764
022205-0333	18.612	15.549	38.052
022205-0335	18.409	15.545	38.000
022305-0320	18.481	15.547	38.049
022305-0323	18.393	15.538	37.920
4075-1912	18.548	15.525	38.013
4076-1854	18.488	15.546	38.149
4079-1811	18.309	15.481	37.722
4079-1815	18.444	15.560	37.989
4082-1651	18.343	15.484	37.748
4082-1702	18.469	15.554	38.100
4082-2002	18.345	15.507	37.809
4082-2008	18.396	15.553	38.012
4085-1935	18.483	15.554	38.083
$\pm 2\sigma$	±0.023	±0.028	±0.093

[a]Pb data are referenced to the following values for NBS-981: 16.937, 15.491, and 36.721 for $^{206}Pb/^{204}Pb$, $^{207}Pb/^{204}Pb$, and $^{208}Pb/^{204}Pb$, respectively (replicate standard analyses yield a mean mass fractionation correction factor of 0.12 ± 0.06%/amu). Error in Pb analyses is dominated by error in the fractionation correction. Maximum blank values for Pb run during the time of these analyses averaged 20 pg.

beneath the Hump Region and is migrating southward [*Mahoney et al.*, 1994]. Similarity in isotopic compositions of PDR TMORB and Hump Region samples, however, suggests this enriched mantle component was already present near 23°S on the SEPR at the time the OSC is thought to have developed.

[32] Sr-Nd-Pb data from Rano Rahi seamount lavas further constrain the nature and timing of the enriched component. Lavas collected from the Rano Rahi seamount field (15–19°S on the SEPR) form mixing arrays in Sr-Nd-Pb space between axial lavas from 13.4°S to 23°S on the SEPR and lavas from the Pukapuka Ridge [*Hall et al.*, 2006]. *Hall et al.* [2006] propose a heterogeneous mantle source for the SEPR consisting of variable amounts of a Pukapuka-like or *C*-type component and within the ambient Pacific NMORB mantle. In the context of evidence that indicates regional eastward flow of the asthenosphere [e.g., *Hammond and Toomey*, 2003], *Hall et al.* [2006] propose that the *C*-rich material was located east of the Pukapuka Ridge system by 5.6 Ma and migrated eastward into the zone of melting, resulting in the eruption of axial and seamount lavas with *C*-like isotopic signatures along a ~500 km section of the SEPR, the length of the Hump Region. Although a comparison to the data of *Hall et al.* [2006] is limited only to Pb isotopes, the PDR TMORB lie along the mixing line between ambient NMORB mantle and the *C*-type Pukapuka end-member in Pb isotope space (Figure 9), suggesting that there was *C*-type material reaching the SEPR axis near 23°S around ~3 Ma. This is consistent with the interpretation of *Hall et al.* [2006], who propose that *C*-type material was present beneath the SEPR axis by this time, although our study extends the area influenced by *C*-type mantle south of the Hump Region.

[33] Interestingly, the second enriched mantle component is clearly observed within the PDR suite as EMORB and associated NMORB, but is absent in zero age lavas from the SEPR. The presence of the EMII-like isotopic signature in the PDR data, and the absence of that signature in the current SEPR data, suggests that this enriched mantle component was exhausted or moved out of the zone of melting over ~3 Ma. The timing of the changes in mantle composition indicated by the PDR and SEPR data sets coincides with the development of the OSC at 20.7°S, which may relate to the development of axial discontinuities, an interesting and significant topic for future research but beyond the scope of this study.

6. Discussion

6.1. Spatial Variability and Implications for Timescales of Magmatic Processes

[34] Timescales of ridge processes can be explored through systematic spatial patterns in the composition of the upper crust. Lavas at the bottom of the extrusive section, for instance, must be older than lavas near the surface. Any systematic trend in lava chemistry with depth therefore implies that lava compositions (and associated magmatic processes) evolve over the time interval required to build the extrusive unit. A strictly temporal interpretation of spatial variability is complicated, of course, by off-axis eruptions [e.g., *Stakes et al.*, 2006] and lateral dike intrusion [e.g., *Stewart et al.*, 2005]. However, the spatial distribution of compositions in the upper crust is the result of accretionary processes operating over time and can therefore provide first-order constraints on the timescales of those processes.

[35] Spatial variations in the compositions of PDR dikes and lavas provide constraints on the evolution of magmatic processes (e.g., melting, mixing, and differentiation) over an extensive range of temporal scales. The longest timescales (i.e., coarsest spatial resolution) are observed in geochemical variations between areas A and B, which are separated by ~14 km (Figure 2). Plate reconstructions (Figure 1) suggest that the crustal sections exposed in areas A and B were generated at a single location, or in close proximity, along the SEPR at approximately 3 Ma [*Naar et al.*, 1991]. Magnetic reversal boundaries at the older extents of the Kaena and Mammoth events intersect areas A and B [*Martinez et al.*, 1991], respectively, implying an age difference between the study areas of ~180 ka, consistent with age calculations based on spreading rate.

[36] Shorter timescales can be observed within areas A and B. Assuming a spreading rate of 72 mm/a (half rate), geochemical variations across each study area (~5 km wide

Figure 9. Lead isotope compositions for selected PDR samples (solid circles), including LREE-depleted MORB (DMORB; blue), NMORB (gray), TMORB (green), and EMORB (red). Data for seamount (squares) and axial (diamonds) lavas (glasses and whole rock) from 13°S to 23°S on the SEPR from *Hamelin et al.* [1984], *Sinton et al.* [1991], *Mahoney et al.* [1994], *Bach et al.* [1994], *Niu et al.* [1996], *Hall et al.* [2006], and *Bergmanis et al.* [2007]. Black symbols indicate seamount EMORB and axial TMORB. Lavas collected between 20.7°S and 23°S are shaded in gray. For fields encompassed by West and East rifts, data are from *Hanan and Schilling* [1989] and *Haase* [2002].

each) represent temporal variations over ~69 ka. The <1-km distance that separates most dive transects corresponds to <14 ka of accretion. Individual dives, which extend vertically (~1 km) through the upper crust, roughly represent the length of time required to accrete the extrusive section. Estimates of the length of time required to build the upper crust are rare, but one approach uses the distance over which seismic layer 2A achieves its full thickness, assuming that layer 2A represents the contact between the extrusive section and the sheeted dike complex [*Christeson et al.*, 1994; *Kent et al.*, 1994; *Vera and Diebold*, 1994]. At 14°15′S on the SEPR (~75 mm/a half rate) layer 2A thickens to a maximum of 500–600 m within roughly two kilometers of the axis, or by ~26 ka [*Kent et al.*, 1994]. Although the correlation of layer 2A to the extrusive-intrusive boundary is controversial, the thickness of layer 2A at 14°15′S approximates the thickness of the PDR extrusive unit and provides a reasonable first-order estimate for the length of time (~26 ka) represented by individual dive transects.

[37] The finest temporal scale of PDR magmatism occurs between closely spaced (<25 m) and adjacent samples. Axial lava flows along the SEPR have estimated thicknesses between ~3 and 12 m [*Sinton et al.*, 2002; *Bergmanis et al.*, 2007], suggesting that adjacent lava samples may be from the same flow and closely spaced lava samples may have captured successive eruptive events. Eruptions along intermediate to superfast spreading centers are thought to be highly episodic, occurring over timescales as short as 10 years or as long as a few hundred years [*Sinton et al.*, 2002; *Bergmanis et al.*, 2007]. Likewise, adjacent and closely spaced dikes represent successive intrusive events that occur on similar timescales. Overall, systematic spatial patterns in the geochemistry of PDR dikes and lavas reveal how magmatic processes at superfast spreading ridges evolve over timescales of tens of years to hundreds of thousands of years.

6.2. Spatial and Temporal Variations in MgO

[38] Evolution of magmatic conditions in the melt lens can be explored through spatial variations in MgO (wt %). Areas A and B generally exhibit similar average MgO (7.8 wt % and 7.3 wt %, respectively), but area A extends to higher values of MgO (9.2 wt % compared to 8.4 wt %) than area B (Figure 2). Area B sampled relatively more dikes (79% of the samples analyzed from area B are dikes) compared to area A (69% of area A samples are dikes), but the difference in chemical variability observed between the two study areas is not the result of biased sampling, as both dikes and lavas extend to higher MgO compositions (Figures 2 and 5).

[39] No systematic trend in MgO occurs within each study area, either with depth or across the width of the exposure. At the Blanco Transform on the Juan de Fuca Ridge, the upward transition of low to high MgO in the extrusive unit has been attributed to the emplacement of lavas off-axis [*Pollock et al.*, 2005]. This interpretation is consistent with strong evidence from the Cleft Segment of the Juan de Fuca Ridge (JdFR) and NEPR that suggests off-axis eruptions play an important role in constructing the extrusive section [e.g., *Stakes et al.*, 2006]. It is difficult to discern the role of off-axis volcanism at the PDR with uncertainties in the axial magmatic setting, but if the upper lavas represent off-axis eruptions, the lack of a predictable change in composition with depth suggests that they are not chemically distinguishable from axial lavas.

[40] Systematic changes in MgO do not appear with depth, but on spatial scales of individual dive transects (~1 km long), MgO concentrations can be relatively consistent (ranging ~1.5 wt %) or highly variable (ranging ~2.5 wt %). For example, *Alvin* dives 4075 (MgO 6.1–8.4 wt %) and 4079 (MgO 5.9–8.5 wt %) from area A and 4084 (MgO 6.0–8.3 wt %) from area B exhibit MgO compositions that span nearly the full range of chemical variability shown by the entire PDR data set (Figure 2). Yet, all samples (9) from *Jason* transect T1 in area B display consistently low MgO (5.9–7.3 wt %) whereas closely spaced samples from *Alvin* dives 4081, 4082, and *Jason* transect T4 (area B) are, in general, moderately evolved (29 samples; MgO 6.8–8.3 wt %; Figure 2). Similar observations can be made in area A, where *Jason* transect T4 shows relatively high MgO samples (11 samples; MgO 7.4–8.8 wt %).

[41] Chemical variability of 2.5 wt % MgO within a ~1 km vertical transect through the dikes and lavas is not surprising, considering that detailed sampling of axial lavas on the SEPR, NEPR, and JdFR show significant variations in MgO [*Sinton et al.*, 1991; *Perfit et al.*, 1994; *Sinton et al.*, 2002; *Bergmanis et al.*, 2007]. Single eruptive units along the SEPR can range up to ~1.2 wt % MgO [*Sinton et al.*, 1991; *Bergmanis et al.*, 2007]. Perhaps more remarkable are the more homogeneous dives, where MgO appears to remain approximately consistent between eruptive events over the time it takes to build the entire thickness of extrusive unit. Interestingly, the transects that are homogeneous (area B T1; 4081, 4082, and area B T4; area A T4) are not consistently high or low in MgO, but rather, occur over the entire range of MgO in the PDR data. On the SEPR, successive eruptive units that show similar distributions of MgO with latitude suggest that magmatic temperatures can remain relatively constant for hundreds of years up to a few tens of thousands of years [*Sinton et al.*, 2002; *Bergmanis et al.*, 2007]. Consistent with these estimates, the PDR dives showing low variability in MgO likely reflect stable magmatic conditions, and because the PDR samples are distributed vertically through the crust, we suggest that magmatic conditions may have been persistent for up to 26 ka. In the context of the extensive seismically detected melt lens [*Detrick et al.*, 1993] and estimates for magma replenishment times on the order of <1000 years [*Rubin and Sinton*, 2007] for fast spreading ridges, it is not unreasonable to imagine that nearly continuous recharge of a stable melt reservoir would lead to magma with relatively consistent MgO compositions over tens of thousands of years.

[42] Most of the crust, however, shows a highly variable, nonsystematic distribution of MgO. MgO was recently demonstrated to be loosely correlated with depth to the axial melt lens along the JdFR and SEPR, where low MgO lavas are associated with the shallowest section of the melt lens and high MgO lavas are located above areas where the melt lens is 100s of meters deeper [*Stakes et al.*, 2006; *Bergmanis et al.*, 2007; *Rubin and Sinton*, 2007]. The relationship between melt lens depth and lava composition has been attributed to the balance between magma supply

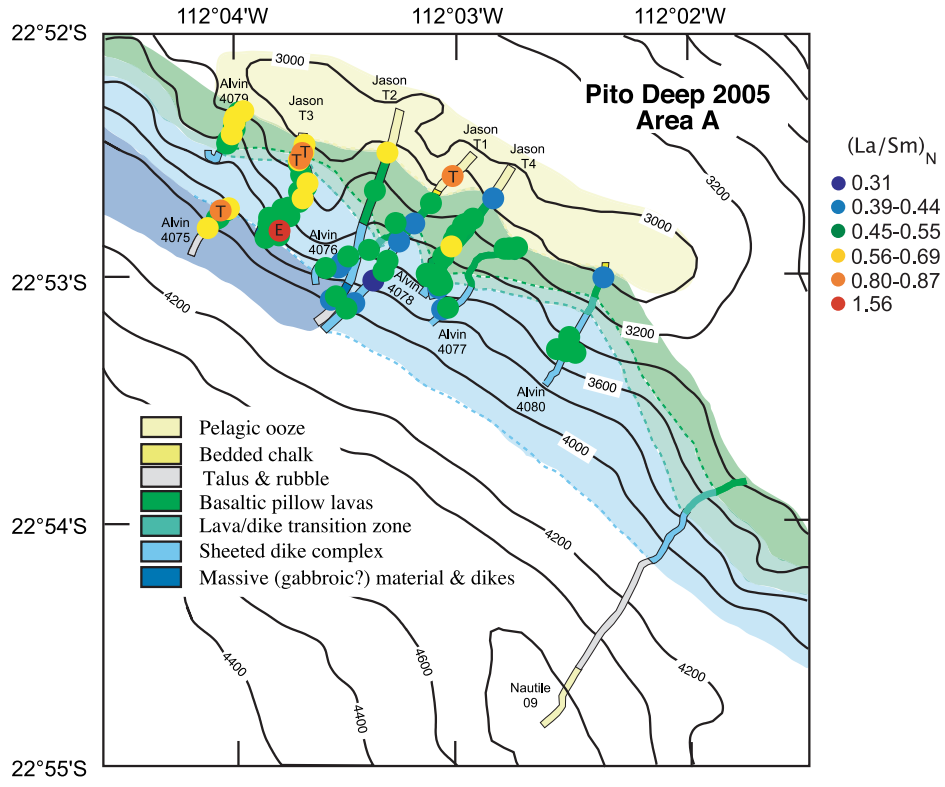

Figure 10. Spatial variations in $(La/Sm)_N$ across area A. EMORB and TMORB are labeled individually. Note that the $(La/Sm)_N$ color bins are distributed unevenly. Green samples represent average NMORB ± 1σ ($(La/Sm)_N$ 0.50 ± 0.05). The most depleted and enriched samples are shown in dark blue and red, respectively. TMORB are indicated by orange circles. Yellow and light blue circles have $(La/Sm)_N$ values higher and lower than NMORB by more than 1σ, respectively. Generally, the more LREE-depleted samples are found in the east and samples less depleted in LREE are located toward the west.

and hydrothermal cooling; the shallowest portions of the melt lens imply high rates of magma recharge, but effective shallow level hydrothermal cooling leads to the eruption of low MgO (low temperature) lavas [*Bergmanis et al.*, 2007; *Rubin and Sinton*, 2007]. If this interpretation is applied to the PDR data, the location of higher MgO samples in area A (compared to area B) implies that hydrothermal cooling may have become less efficient and the melt lens may have deepened over ~180 ka. Unfortunately, there is no systematic change in MgO across each study area, nor in the degree of hydrothermal alteration between areas A and B [*Heft et al.*, 2008], to support this interpretation. Therefore, 1 wt % difference in maximum MgO between areas A and B likely does not reflect the long-term evolution of the hydrothermal magma supply system. Rather, the high MgO samples may reflect more local time-space variations in magmatic processes, such as rapidly evolving melt reservoirs [e.g., *Bergmanis et al.*, 2007], mantle melts that bypass the axial melt lens [e.g., *Rubin and Sinton*, 2007], or along-axis transport and eruption of chemically distinct magma [e.g., *Stewart et al.*, 2005].

6.3. Spatial and Temporal Variations in Indicators of Mantle Source Composition

[43] Patterns in trace element ratios and Pb isotopes suggest that the PDR dikes and lavas were generated from a heterogeneous three-component mantle. Our discussion of the evolution of source composition focuses on area A, which, compared to area B, shows a significantly greater diversity in indicators of mantle source composition, including samples that are the most depleted ($(La/Sm)_N$ 0.31), most enriched ($(La/Sm)_N$ 1.56), and transitional in $(La/Sm)_N$ (Figures 8 and 10). Within area A, the low $(La/Sm)_N$ (<0.45) samples are generally located in the east whereas the higher $(La/Sm)_N$ (>0.55) samples fall toward the west (Figure 10). The distribution of $(La/Sm)_N$ across the width of the study area suggests that either a mantle more enriched in LREE moved into the zone of melting or the mantle evolved toward a more LREE-enriched composition over a period of roughly 69 ka.

[44] Further constraints on the timing of source composition evolution are revealed in the distribution of Pb isotopes. The EMORB (020905–1404) and three of the four area A TMORB ($^{206}Pb/^{204}Pb$ > 18.5; 4075–1912, 021105–0627, 021105–0639) are located within Alvin dive 4075 and Jason transect T3 (Figure 10). Together, these dives cover a narrow (~0.5 km wide) strip of the scarp, representing ~7 ka of accretion based on spreading rate. Recall that EMORB and TMORB represent two separate and distinct enriched mantle sources, so their presence in such a restricted area suggests that melts from both enriched sources contributed to crustal accretion nearly simultaneously. Although Pb isotopes were not measured for the entire sample suite, only one TMORB (020805–0108) was

recovered outside of dives 4075 and T3, suggesting that melt from the TMORB source was largely intruded and erupted at this location along the SEPR over a very limited period of time (~7 ka).

[45] A simple explanation for the limited spatial distribution of TMORB is that the TMORB source mantle was present in the zone of melting for only tens of thousands of years. This is not an unreasonable estimate, considering that chemical heterogeneity within individual lava flows on the present-day SEPR require rapid variations in source composition over timescales of hundreds of years [*Bergmanis et al.*, 2007]. In this context, one might expect the upper crust to be heterogeneous in terms of mantle source indicators on spatial scales of individual eruptive events, or tens of meters. Rapid evolution of the mantle over tens of thousands of years could thus explain the limited spatial distribution of PDR TMORB. It is likely, however, that some of the compositional variability reflects along-axis spatial variations that are preserved in the dikes and lavas through along-axis magma transport and eruption.

6.4. Adjacent Samples and Implications for Horizontal Magma Transport

[46] To further examine the dynamic nature of the axial magmatic system, observations can be made of adjacent and closely spaced samples. An unprecedented 10 lavas and 42 dikes were collected within 25 m of each other while an additional 19 adjacent dikes (4 from area A and 15 from area B) were also recovered. Some closely spaced samples are chemically similar or only differ in extent of crystallization (e.g., adjacent dikes 4079–1811 and 1815; Figure 11). Single lava flows from intermediate to fast spreading ridges (JdFR, NEPR, and SEPR) have been shown to be more chemically homogeneous than individual lava flows from slower spreading ridges [e.g., *Rubin et al.*, 2001; *Sinton et al.*, 2002]. Thus, compositional homogeneity of closely spaced samples of lavas from the PDR is not surprising, and may suggest that some of the closely spaced samples were recovered from the same lava flow or were erupted contemporaneously from the same melt reservoir. The same inference may be made, then, for chemically similar dikes. Not only may they have been intruded nearly simultaneously, but adjacent dikes showing compositional homogeneity suggest an origin from the same melt reservoir.

[47] In terms of chemical composition, however, many of the closely spaced dike samples exhibit differences in composition that are inconsistent with simple crystallization from a common parental magma (e.g., adjacent dikes 4082–1814 and 1820; Figure 11). For example, on plots of major element variations with MgO, tie lines connect adjacent dikes that cross the modeled liquid lines of descent. Similar discordant relationships can also be observed in incompatible trace element ratios (Figure 11), which indicate that spatially proximate samples can show significant differences in source composition. Considering along-axis chemical variability in the melt lens [e.g., *Mahoney et al.*, 1994], the wide range in spatial scales for individual lava flows (<1 to >19 km^2 [*Sinton et al.*, 2002]), and the periodicity of axial eruptions (tens to hundreds of years [*Bergmanis et al.*, 2007]), it is logical that chemically distinct lava flows may often be emplaced within the same segment [*Sinton et al.*, 2002] and that multiple parental magmas may contribute to a single lava flow [*Bergmanis et al.*, 2007]. Because chemically heterogeneous eruptions can be closely associated in space and time, it follows that the feeder dikes for these eruptions should show a high degree of chemical variability over short spatial (and temporal scales) as well.

[48] The high degree of compositional variability displayed by PDR dikes over short spatial (and inferred temporal) scales is comparable to the extent of variability observed in adjacent dike pairs from the Hess Deep Rift [*Stewart et al.*, 2002]. Several Hess Deep dike pairs show patterns in major and trace elements that indicate different parental sources [*Stewart et al.*, 2002]. This observation led to a model for crustal accretion in which magma from chemically distinct melt reservoirs intrudes as dikes and is transported laterally along axis over short timescales, resulting in the juxtaposition of chemically distinct magmas in adjacent dikes [*Stewart et al.*, 2002]. This model is consistent with multiple studies of magmatic flow textures [e.g., *Staudigel et al.*, 1992; *Varga et al.*, 1998] and seismic activity [*Dziak et al.*, 1995; *Embley et al.*, 2000; *Dziak et al.*, 2007], demonstrating the importance of lateral propagation of dikes.

[49] Although there is much evidence for lateral dike propagation, there are strong indications that magma transport at 17°30′S on the SEPR is predominantly vertical [*Bergmanis et al.*, 2007]. Systematic along-axis variations in lava compositions that correlate with the location of a third-order discontinuity and depth to the seismic melt lens reflector suggest that the lavas represent the chemistry of the underlying melt reservoir. Highly variable lava compositions exist in close proximity in space and time without the need to invoke lateral magma transport from chemically distinct segments of the melt lens. This model has implications for chemical variability within dikes, specifically, that adjacent dikes of variable composition can be juxtaposed as a result of vertical magma transport from a rapidly evolving melt lens. *Bergmanis et al.* [2007] acknowledge that lateral magma transport may indeed occur at other locations, but the unusually shallow (~1 km depth) melt lens at 17°30′S promotes vertical dike propagation and eruption.

[50] Given that models for vertical and lateral magma transport both predict the intrusion of chemically distinct dikes over short spatial and temporal scales, it is necessary to evaluate the PDR data in the context of other evidence for the direction of magma transport. Flow directions obtained through anisotropy of magnetic susceptibility (AMS) have been shown to correlate with other macroscopic and microscopic magmatic flow indicators [e.g., *Knight and Walker*, 1988; *MacDonald and Palmer*, 1990; *Varga et al.*, 1998]. Direct evidence for lateral magma transport comes from a study of PDR dikes by *Varga et al.* [2008], who are the first to report on AMS fabrics from fully oriented in situ dike samples. PDR dikes show a characteristic remanent magnetization that is consistent with a two-stage rotation model in which dikes are initially rotated about a horizontal axis by normal faulting near the ridge followed by a clockwise rotation about a vertical axis as a result of the rotation of the Easter Microplate. PDR dikes were restored to their original orientation using the two-stage rotation model so that AMS fabrics could be properly interpreted. Flow directions were determined from AMS fabrics based on the orientation of

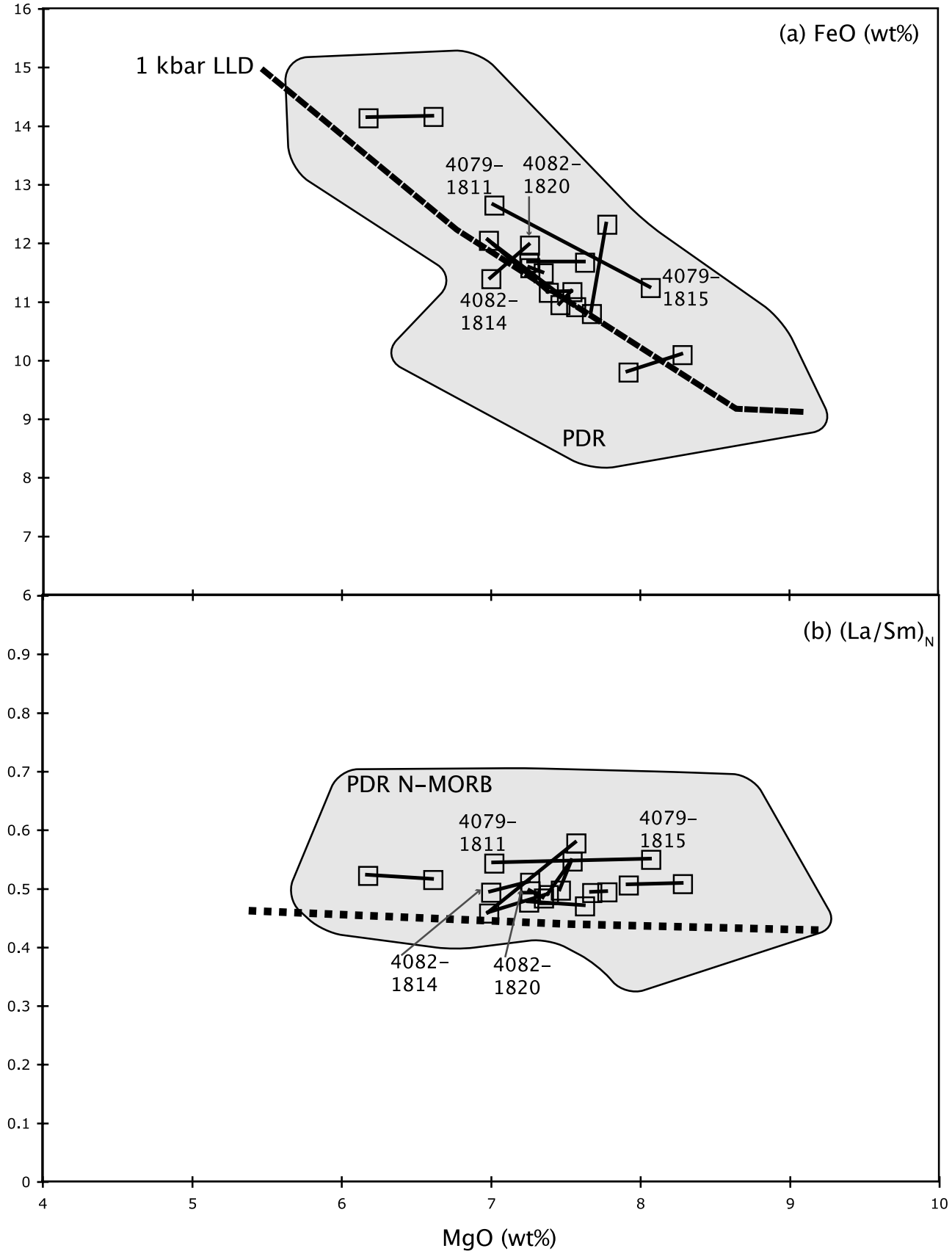

Figure 11. Variations in (a) FeO* (wt %) and (b) $(La/Sm)_N$ versus MgO (wt %) for adjacent dikes, joined by tie lines. Effects of low-pressure crystallization shown by the 1 kbar LLD (dotted line). Gray field indicates the range of all PDR samples in Figure 11a and PDR NMORB in Figure 11b.

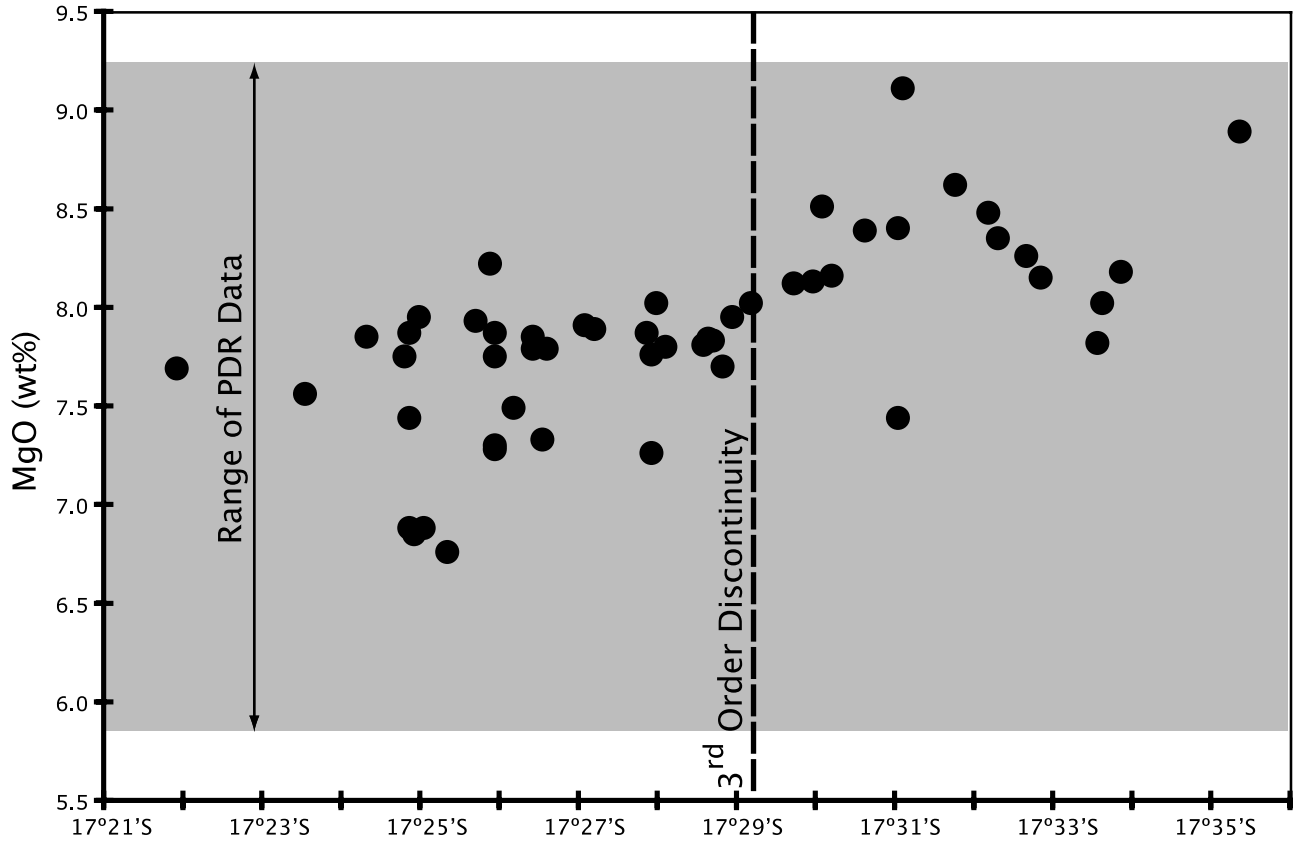

Figure 12. MgO (wt %) versus latitude for whole rock samples from the 17°30′S area of the SEPR from *Bergmanis et al.* [2007]. South of the third-order discontinuity at ∼17°29′S, high MgO (high temperature) lavas correspond to a region of relatively weaker magma supply, as indicated by a deepening melt lens reflector. High variability and high MgO values in the PDR data, as shown by the gray field, suggest that the setting for the PDR may have been analogous to the axial region south of the discontinuity.

the maximum principal susceptibility, which is dominantly dike-parallel and shallowly plunging in the PDR dikes. With respect to the original orientation, AMS fabrics in the PDR dikes suggest that magma flow was predominantly horizontal and parallel to the SEPR axis [*Horst et al.*, 2006; *Varga et al.*, 2008]. In light of the AMS data, we prefer the lateral dike transport model.

[51] It may be significant to consider whether the role of lateral dike propagation changes depending on location along the ridge segment. This can be examined by comparing the compositions of PDR samples to the SEPR data of *Bergmanis et al.* [2007], where MgO has been shown to correlate with depth to the melt lens and inferred rate of magma recharge. Overall, the PDR crust shows more variability in MgO compared to the SEPR data (Figure 12), extending across a range of compositions even greater than those observed south of the third-order discontinuity at ∼17°29′S. South of this boundary, high-temperature (high MgO) lavas are erupted over a deep (∼1300 m) melt lens, implying that this portion of the ridge has a relatively smaller volume of magma supply than the adjacent segment to the north. The high degree of variability in PDR compositions resembles data from south of 17°29′S, suggesting that the PDR may have formed under conditions analogous to a segment end, where magma supply is relatively restricted.

[52] AMS fabrics in PDR dikes and the high degree of variability between adjacent dike pairs suggest that lateral magma transport occurs beneath superfast spreading centers. However, in the model proposed by *Bergmanis et al.* [2007], dikes intrude vertically, erupting low MgO lava at segment centers and high MgO lava at segment ends. Indeed, axial variations in MgO near 17°30′S are best explained by vertical dike intrusion, even in regions of restricted magma supply comparable to segment ends. The relative importance of lateral and vertical magma transport may depend on segment location. Our preference for the lateral magma transport model to explain the PDR data does not refute that dikes at segment centers may be emplaced through vertical propagation. Rather, our findings suggest that vertical dike intrusion at segment ends is possible, but most segment end dikes are emplaced through lateral intrusion. This adds an important three-dimensional perspective to the conceptual model for the formation of the upper crust, in which mantle melts are focused toward the segment center where dikes originate and laterally transport magma along axis toward the segment ends.

7. Conclusions

[53] Chemical analyses of dikes and lavas from the Pito Deep Rift reveal insights into the processes of crustal accretion and evolution at superfast rate spreading centers. The longest-term changes (∼3 Ma) are observed in comparisons of Pb isotopes and trace element ratios between PDR

and zero age lavas from the SEPR, which indicate a variably enriched mantle that has evolved over time to become more depleted in one of the enriched components. The limited spatial distribution of TMORB and the occurrence of homogeneous MgO compositions over scales of ~1 km suggests that the mantle source composition evolved and magmatic temperatures persisted over timescales of tens of thousands of years. These estimates are consistent with previous estimates for the evolution of magmatic processes, but it is likely that some of the spatial variability results from along-axis transport of magma from a melt lens that is chemically and/or physically segmented along strike. Indeed, the PDR crust is heterogeneous at spatial scales on the order of meters (and timescales of tens to hundreds of years), consistent with patterns in AMS fabrics that support along-axis propagation of dikes. This finding contrasts with a recent model for crustal accretion that suggests that dike transport is likely to occur vertically at superfast spreading centers, a setting thought to characterize the ridge axis where PDR crust formed. Clearly, observations from tectonic windows, and the unique cross-sectional perspective provided by the PDR in particular, provide valuable insights and offer significant contributions to advancing our understanding of oceanic crustal accretion.

[54] **Acknowledgments.** The manuscript benefited greatly from careful reviews by Mike Perfit, John Sinton, and Associate Editor Allegra Hosford Scheirer. We would like to thank the captain and crew of *Atlantis II* and WHOI-DSOG. We are grateful to the scientific party of cruise AT11-23. We are would also like to thank G. Dwyer and S. Ogburn for the help with the analyses. This work was supported by the U.S. National Science Foundation (NSF-OCE 0222154 and NSF-OCE-RIDGE2000 0526120).

References

Alt, J. C. (1993), Low-temperature alteration of basalts from the Hawaiian Arch, Leg 136, *Proc. Ocean Drill. Program Sci. Results*, *136*, 133–146.

Andrews, A. J. (1977), Low temperature fluid alteration of oceanic layer 2 basalts, DSDP Leg 37, *Can. J. Earth Sci.*, *14*, 911–926.

Asimow, P. D., and M. S. Ghiorso (1998), Algorithmic modifications extending MELTS to calculate subsolidus phase relations, *Am. Mineral.*, *83*, 1127–1132.

Bach, W., E. Hegner, J. Erzinger, and M. Satir (1994), Chemical and isotopic variations along the superfast spreading East Pacific Rise from 6 to 30°S, *Contrib. Mineral. Petrol.*, *116*, 365–380, doi:10.1007/BF00310905.

Bedard, J. H. (1994), A procedure for calculating the equilibrium distribution of trace elements among the minerals of cumulate rocks, and the concentration of trace elements in the coexisting liquids, *Chem. Geol.*, *118*, 143–153, doi:10.1016/0009-2541(94)90173-2.

Bergmanis, E. C., J. Sinton, and K. H. Rubin (2007), Recent eruptive history and magma reservoir dynamics on the southern East Pacific Rise at 17°30′S, *Geochem. Geophys. Geosyst.*, *8*, Q12O06, doi:10.1029/2007GC001742.

Byerly, G. (1980), The nature of differentiation trends in some volcanic rocks from the Galapagos spreading center, *J. Geophys. Res.*, *85*, 3797–3810, doi:10.1029/JB085iB07p03797.

Cheatham, M., W. F. Sangrey, and W. M. White (1993), Sources of error in external calibration ICP-MS analysis of geological samples and improved nonlinear drift correction procedure, *Spectrochim. Acta B*, *48*, 487–506.

Christeson, G. L., G. M. Purdy, and G. J. Fryer (1994), Seismic constraints on shallow crustal emplacement processes at the fast spreading East Pacific Rise, *J. Geophys. Res.*, *99*, 17,957–17,973, doi:10.1029/94JB01252.

Christeson, G. L., K. D. McIntosh, and J. A. Karson (2007), Inconsistent correlation of seismic layer 2a and lava layer thickness in oceanic crust, *Nature*, *445*, 418–421, doi:10.1038/nature05517.

Cogne, J. P., J. Francheteau, V. Courtillot, and Pito93 Scientific Team (1995), Large rotation of the Easter Microplate as evidenced by oriented paleomagnetic samples from the ocean floor, *Earth Planet. Sci. Lett.*, *136*, 213–222, doi:10.1016/0012-821X(95)00191-E.

Constantin, M., R. Hekinian, D. Bideau, and R. Hebert (1996), Construction of the oceanic lithosphere by magmatic intrusions; petrological evidence from plutonic rocks formed along the fast-spreading East Pacific Rise, *Geology*, *24*, 731–734, doi:10.1130/0091-7613(1996)024<0731:COTOLB>2.3.CO;2.

Cormier, M.-H., and K. C. Macdonald (1994), East Pacific Rise 18°–19°S: Asymmetric spreading and ridge reorientation by ultrafast migration of axial discontinuities, *J. Geophys. Res.*, *99*, 543–564, doi:10.1029/93JB02382.

Danyushevsky, L. V. (2001), The effect of small amounts of H_2O on crystallization of mid-ocean ridge and backarc basin magmas, *J. Volcanol. Geotherm. Res.*, *110*(3–4), 265–280, doi:10.1016/S0377-0273(01)00213-X.

Detrick, R. S., A. J. Harding, G. M. Kent, J. A. Orcutt, J. C. Mutter, and P. Buhl (1993), Seismic structure of the southern East Pacific Rise, *Science*, *259*, 499–503, doi:10.1126/science.259.5094.499.

Dziak, R. P., C. G. Fox, and A. E. Schreiner (1995), The June–July 1993 seismo-acoustic event at CoAxial segment, Juan de Fuca Ridge: Evidence for a lateral dike injection, *Geophys. Res. Lett.*, *22*, 135–138, doi:10.1029/94GL01857.

Dziak, R. P., D. R. Bohnenstiehl, J. P. Cowen, E. T. Baker, K. H. Rubin, J. H. Hazel, and M. J. Fowler (2007), Rapid dike emplacement leads to dramatic hydrothermal plume release during seafloor spreading events, *Geology*, *35*, 579–582, doi:10.1130/G23476A.1.

Embley, R. W., W. W. Chadwick, M. R. Perfit, M. C. Smith, and J. R. Delaney (2000), Recent eruptions on the CoAxial segment of the Juan de Fuca Ridge: Implications for mid-ocean ridge accretion processes, *J. Geophys. Res.*, *105*, 16,501–16,525, doi:10.1029/2000JB900030.

Francheteau, J., D. Naar, R. Armijo, J.-P. Cogne, M. Constantin, J. Girardeau, R. Hekinian, R. Hey, and R. Searle (1994), Black smoker discovered, Pito Seamount near Easter Microplate propagator tip, *Eos Trans. AGU*, *75*(16), Spring Meet. Suppl., 322.

Gast, P. W. (1968), Trace element fractionation and the origin of tholeiitic and alkaline magma types, *Geochim. Cosmochim. Acta*, *32*, 1057–1068, doi:10.1016/0016-7037(68)90108-7.

Ghiorso, M. S., and R. O. Sack (1995), Chemical mass transfer in magmatic processes IV. A revised and internally consistent thermodynamic model for the interpolation and extrapolation of liquid-solid equilibria in magmatic systems at elevated temperatures and pressures, *Contrib. Mineral. Petrol.*, *119*, 197–212, doi:10.1007/BF00307281.

Green, T. H., and A. E. Ringwood (1968), Genesis of the calc-alkaline igneous rock suite, *Contrib. Mineral. Petrol.*, *18*(2), 105–162, doi:10.1007/BF00371806.

Haase, K. M. (2002), Geochemical constraints on magma sources an mixing processes in Easter Microplate MORB (SE Pacific): A case study of plume-ridge interaction, *Chem. Geol.*, *182*, 335–355, doi:10.1016/S0009-2541(01)00327-8.

Hall, L. S., J. J. Mahoney, J. M. Sinton, and R. A. Duncan (2006), Spatial and temporal distribution of a C-like asthenospheric component in the Rano Rahi Seamount Field, East Pacific Rise, 15°–19°S, *Geochem. Geophys. Geosyst.*, *7*, Q03009, doi:10.1029/2005GC000994.

Hamelin, B., B. Dupre, and J. Allegre (1984), Lead-strontium isotopic variations along the East Pacific Rise and the Mid-Atlantic Ridge, *Earth Planet. Sci. Lett.*, *67*, 340–350, doi:10.1016/0012-821X(84)90173-0.

Hammond, W. C., and D. R. Toomey (2003), Seismic velocity anisotropy and heterogeneity beneath the Mantle Electromagnetic and Tomography Experiment (MELT) region of the East Pacific Rise from analysis of *P* and *S* body waves, *J. Geophys. Res.*, *108*(B4), 2176, doi:10.1029/2002JB001789.

Hanan, B. B., and J.-G. Schilling (1989), Easter Microplate evolution: Pb isotope evidence, *J. Geophys. Res.*, *94*, 7432–7448, doi:10.1029/JB094iB06p07432.

Handschumacher, D. W., R. H. Pilger, J. A. Forman, and J. F. Campbell (1981), Structure and evolution of the Easter plate, in *Nazca Plate: Crustal Formation and Andean Convergence*, edited by L. Kulm et al., *Mem. Geol. Soc. Am.*, *154*, 63–76.

Hayman, N. W., and J. A. Karson (2006), Fault-controlled fluid flow regimes along the East Pacific Rise (EPR): Geologic views through tectonic windows, *Geol. Soc. Am. Abstr. Programs*, *38*, 17.

Heft, K. L., K. M. Gillis, M. A. Pollock, J. A. Karson, and E. M. Klein (2008), Role of upwelling hydrothermal fluids in the development of alteration patterns at fast spreading ridges: Evidence from the sheeted dike complex at Pito Deep, *Geochem. Geophys. Geosyst.*, *9*, Q05O07, doi:10.1029/2007GC001926.

Hekinian, R., J. Francheteau, R. Armijo, J.-P. Cogné, M. Constantin, J. Girardeau, R. Hey, D. Naar, and R. Searle (1996), Petrology of the Easter Microplate region in the South Pacific, *J. Volcanol. Geotherm. Res.*, *72*, 259–289, doi:10.1016/0377-0273(96)00013-3.

Hey, R. N., D. F. Naar, M. C. Kleinrock, W. J. Phipps Morgan, E. Morales, and J. G. Schilling (1985), Microplate tectonics along a superfast seafloor spreading system near Easter Island, *Nature*, *317*, 320–325, doi:10.1038/317320a0.

Horst, A., R. J. Varga, J. S. Gee, and J. A. Karson (2006), Magnetic remanence and anisotropy of magnetic susceptibility of dikes from super-fast spread crust exposed at Pito Deep Rift, *Eos Trans. AGU*, *87*(52), Fall Meet. Suppl., Abstract T51C-1546.

Humphris, S., W. Melson, and R. Thompson (1980), Basalt weathering on the East Pacific Rise and the Galapagos spreading center, Deep Sea Drilling Project Leg 54, *Deep Sea Drill. Proj. Initial Rep.*, *54*, 773–787.

Karson, J. A., et al. (2002a), Structure of uppermost fast-spread oceanic crust exposed at the Hess Deep Rift: Implications for subaxial processes at the East Pacific Rise, *Geochem. Geophys. Geosyst.*, *3*(1), 1002, doi:10.1029/2001GC000155.

Karson, J. A., M. A. Tivey, and J. R. Delaney (2002b), Internal structure of uppermost oceanic crust along the Western Blanco Transform Scarp: Implications for subaxial accretion and deformation at the Juan de Fuca Ridge, *J. Geophys. Res.*, *107*(B9), 2181, doi:10.1029/2000JB000051.

Karson, J. A., et al. (2005), Nested-scale investigation of tectonic windows into super-fast spread crust exposed at the Pito Deep Rift, Easter Microplate, SE Pacific, *InterRidge Newsl.*, *14*, 5–8.

Kent, G. M., A. J. Harding, J. A. Orcutt, R. S. Detrick, J. C. Mutter, and P. Buhl (1994), Uniform accretion of oceanic crust south of the Garrett transform at 14°15′S on the East Pacific Rise, *J. Geophys. Res.*, *99*, 9097–9116, doi:10.1029/93JB02872.

Klein, E. M., and C. H. Langmuir (1987), Global correlations of ocean ridge basalt chemistry with axial depth and crustal thickness, *J. Geophys. Res.*, *92*, 8089–8115, doi:10.1029/JB092iB08p08089.

Klein, E. M., C. H. Langmuir, and H. Staudigel (1991), Geochemistry of basalts from the Southeast Indian Ridge, 115°E–138°E, *J. Geophys. Res.*, *96*, 2089–2107, doi:10.1029/90JB01384.

Knight, M. D., and G. P. L. Walker (1988), Magma flow directions in dikes of the Koolau Complex, Oahu, determined from magnetic fabric studies, *J. Geophys. Res.*, *93*, 4301–4320, doi:10.1029/JB093iB05p04301.

Larson, R. L., C. T. Popham, and R. A. Pockalny (2005), Lithologic and structural observations at Endeavor Deep and their implications for the accretion process at fast to ultra-fast spreading rates, *Eos Trans. AGU*, *86*(52), Fall Meet. Suppl., Abstract T33D-0594.

Macdonald, K. C., R. M. Haymon, S. P. Miller, J.-C. Sempere, and P. J. Fox (1988), Deep-tow and SeaBeam studies of dueling propagating ridges on the East Pacific Rise near 20°40′S, *J. Geophys. Res.*, *93*, 2875–2898, doi:10.1029/JB093iB04p02875.

MacDonald, W. D., and H. C. Palmer (1990), Flow directions in ash-flow tuffs: A comparison of geologic and magnetic susceptibility measurement, Tshirege member (upper Bandelier Tuff), Valles caldera, New Mexico, USA, *Bull. Volcanol.*, *53*, 45–59, doi:10.1007/BF00680319.

Mahoney, J. J., J. M. Sinton, M. D. Kurz, J. D. MacDougall, K. J. Spencer, and G. W. Lugmair (1994), Isotope and trace element characteristics of a superfast spreading ridge: East Pacific Rise 13–23°S, *Earth Planet. Sci. Lett.*, *121*, 173–191, doi:10.1016/0012-821X(94)90039-6.

Martinez, F., D. F. Naar, T. B. Reed IV, and R. N. Hey (1991), Three-dimensional SeaMARC II, gravity, and magnetics study of large-offset rift propagation at the Pito rift, Easter Microplate, *Mar. Geophys. Res.*, *13*, 255–285, doi:10.1007/BF00366279.

Moores, E. M., and F. J. Vine (1971), The Troodos massif, Cyprus, and other ophiolites as oceanic crust: Evaluation and implications, *Philos. Trans. R. Soc. London, Ser. A*, *268*, 443–466, doi:10.1098/rsta.1971.0006.

Morgan, L. A., J. A. Karson, N. W. Hayman, R. J. Varga, and S. D. Hurst (2005), Internal structure of basaltic lavas and sheeted dikes in 3 Ma super-fast EPR crust exposed at Pito Deep, *Eos Trans. AGU*, *86*(52), Fall Meet. Suppl., Abstract T33D-0588.

Naar, D. F., and R. N. Hey (1989), Speed limit for oceanic transform faults, *Geology*, *17*, 420–422, doi:10.1130/0091-7613(1989)017<0420:SLFOTF>2.3.CO;2.

Naar, D. F., and R. N. Hey (1991), Tectonic evolution of the Easter Microplate, *J. Geophys. Res.*, *96*, 7961–7993, doi:10.1029/90JB02398.

Naar, D. F., F. Martinez, R. N. Hey, T. B. Reed IV, and S. Stein (1991), Pito rift: How a large-offset rift propagates, *Mar. Geophys. Res.*, *13*, 287–309, doi:10.1007/BF00366280.

Niu, Y., D. G. Waggoner, J. M. Sinton, and J. J. Mahoney (1996), Mantle source heterogeneity and melting processes beneath seafloor spreading centers: East Pacific Rise 18°–19°S, *J. Geophys. Res.*, *101*, 27,711–27,733, doi:10.1029/96JB01923.

Parrish, R. R., J. C. Roddick, W. D. Loveridge, and R. W. Sullivan (1987), Uranium-lead analytical techniques at the Geochronology Laboratory, *Pap. Geol. Surv. Can.*, *82*, 3–7.

Perfit, M. R., D. J. Fornari, M. C. Smith, J. F. Bender, C. H. Langmuir, and R. M. Haymon (1994), Small-scale spatial and temporal variations in mid-ocean ridge crest magmatic processes, *Geology*, *22*, 375–379, doi:10.1130/0091-7613(1994)022<0375:SSSATV>2.3.CO;2.

Perk, N. W., L. A. Coogan, J. A. Karson, E. M. Klein, and H. Hanna (2007), Petrology and geochemistry of primitive lower oceanic crust from Pito Deep: Implications for the accretion of the lower crust at the southern East Pacific Rise, *Contrib. Mineral. Petrol.*, *154*(5), doi:10.1007/s00410-007-0210-z.

Pollock, M. A. (2007), Geochemistry of dikes and lavas from tectonic windows, Ph.D. dissertation, Duke Univ., Durham, N. C.

Pollock, M. A., E. M. Klein, J. A. Karson, and M. A. Tivey (2005), Temporal and spatial variability in the composition of lavas exposed along the Western Blanco Transform Fault, *Geochem. Geophys. Geosyst.*, *6*, Q11009, doi:10.1029/2005GC001026.

Rapanui Scientific Party, et al. (1988), Pito and Orongo fracture zones: The northern and southern boundaries of the Easter Microplate (southeast Pacific), *Earth Planet. Sci. Lett.*, *89*, 363–374, doi:10.1016/0012-821X(88)90123-9.

Rubin, K. H., and J. M. Sinton (2007), Inferences on mid-ocean ridge thermal and magmatic structure from MORB compositions, *Earth Planet. Sci. Lett.*, *260*, 257–276, doi:10.1016/j.epsl.2007.05.035.

Rubin, K. H., M. C. Smith, E. C. Bergmanis, M. R. Perfit, J. M. Sinton, and R. Batiza (2001), Magmatic history and volcanological insights from individual lava flows erupted on the seafloor, *Earth Planet. Sci. Lett.*, *188*, 349–367, doi:10.1016/S0012-821X(01)00339-9.

Rusby, R. I., and R. C. Searle (1993), Intraplate thrusting near the Easter Microplate, *Geology*, *21*, 311–314, doi:10.1130/0091-7613(1993)021<0311:ITNTEM>2.3.CO;2.

Rusby, R. I., and R. C. Searle (1995), A history of the Easter Microplate, 5.25 Ma to present, *J. Geophys. Res.*, *100*(B7), 12,617–12,640, doi:10.1029/94JB02779.

Searle, R. C., R. I. Rusby, J. Engeln, R. N. Hey, J. Zukin, P. M. Hunter, T. P. LeBas, H. J. Hoffman, and R. Livermore (1989), Comprehensive sonar imaging of the Easter Microplate, *Nature*, *341*, 701–705, doi:10.1038/341701a0.

Sempéré, J.-C., K. C. Macdonald, S. P. Miller, and L. Shure (1987), Detailed study of the Brunhes/Matuyama reversal boundary on the east Pacific rise at 19°30′S: Implications for crustal emplacement processes at an ultra fast spreading center, *Mar. Geophys. Res.*, *9*, 1–23, doi:10.1007/BF00338248.

Sims, K. W., et al. (2002), Chemical and isotopic constraints on the generation and transport of magma beneath the East Pacific Rise, *Geochim. Cosmochim. Acta*, *66*, 3481–3504, doi:10.1016/S0016-7037(02)00909-2.

Sinton, J. M., and P. Fryer (1987), Mariana trough lavas from 18°N: Implications for the origin of back-arc basin basalts, *J. Geophys. Res.*, *92*, 12,782–12,802, doi:10.1029/JB092iB12p12782.

Sinton, J. M., S. M. Smaglick, J. J. Mahoney, and K. C. Macdonald (1991), Magmatic processes at superfast spreading mid-ocean ridges: Glass compositional variations along the East Pacific Rise 13°–23°S, *J. Geophys. Res.*, *96*, 6133–6155, doi:10.1029/90JB02454.

Sinton, J., E. Bergmanis, K. Rubin, R. Batiza, T. K. P. Gregg, K. Grönvold, K. C. Macdonald, and S. M. White (2002), Volcanic eruptions on mid-ocean ridges: New evidence from the superfast spreading East Pacific Rise, 17°–19°S, *J. Geophys. Res.*, *107*(B6), 2115, doi:10.1029/2000JB000090.

Sisson, T. W., and T. L. Grove (1993), Experimental investigations of the role of H_2O in calc-alkaline differentiation and subduction zone magmatism, *Contrib. Mineral. Petrol.*, *113*(2), 143–166, doi:10.1007/BF00283225.

Stakes, D. S., M. R. Perfit, M. A. Tivey, D. W. Caress, T. M. Ramirez, and N. Maher (2006), The Cleft revealed: Geologic, magnetic, and morphologic evidence for construction of upper oceanic crust along the southern Juan de Fuca Ridge, *Geochem. Geophys. Geosyst.*, *7*, Q04003, doi:10.1029/2005GC001038.

Staudigel, H., J. S. Gee, L. Tauxe, and R. J. Varga (1992), Shallow intrusive directions of sheeted dikes in the Troodos ophiolite, *Geology*, *20*, 841–844, doi:10.1130/0091-7613(1992)020<0841:SIDOSD>2.3.CO;2.

Stewart, M. A., E. M. Klein, and J. A. Karson (2002), Geochemistry of dikes and lavas from the north wall of the Hess Deep Rift: Insights into the four-dimensional character of crustal construction at fast spreading mid-ocean ridges, *J. Geophys. Res.*, *107*(B10), 2238, doi:10.1029/2001JB000545.

Stewart, M. A., E. M. Klein, J. A. Karson, and J. G. Brophy (2003), Geochemical relationships between dikes and lavas at the Hess Deep Rift: Implications for magma eruptibility, *J. Geophys. Res.*, *108*(B4), 2184, doi:10.1029/2001JB001622.

Stewart, M. A., J. A. Karson, and E. M. Klein (2005), Four-dimensional upper crustal construction at fast-spreading mid-ocean ridges: A perspective from an upper crustal cross-section at the Hess Deep Rift, *J. Volcanol. Geotherm. Res.*, *144*, 287–309, doi:10.1016/j.jvolgeores.2004.11.026.

Sun, S.-S., and W. F. McDonough (1989), Chemical and isotopic systematics of oceanic basalts: Implications for mantle composition and process, in *Magmatism in the Ocean Basins*, edited by A. D. Saunder and M. J. Norry, *Geol. Soc. Spec. Publ.*, *42*, 3313–3345.

Tivey, M. A., H. P. Johnson, C. Fleutelot, S. Hussenoeder, R. Lawrence, C. Waters, and B. Wooding (1998), Direct measurement of magnetic

reversal polarity boundaries in a cross-section of oceanic crust, *Geophys. Res. Lett.*, *25*, 3631–3634, doi:10.1029/98GL02752.

Varga, R. J., J. Gee, and H. Staudigel (1998), Dike surface lineations as magma flow indicators within the sheeted dike complex of the Troodos ophiolite, Cyprus, *J. Geophys. Res.*, *103*, 5241–5256, doi:10.1029/97JB02717.

Varga, R. J., A. J. Horst, J. S. Gee, and J. A. Karson (2008), Direct evidence from anisotropy of magnetic susceptibility for lateral melt migration at superfast spreading centers, *Geochem. Geophys. Geosyst.*, *9*, Q08008, doi:10.1029/2008GC002075.

Vera, E. E., and J. B. Diebold (1994), Seismic imaging of oceanic layer 2A between 9°30′N and 10°N on the East Pacific Rise from two-ship wide-aperture profiles, *J. Geophys. Res.*, *99*, 3031–3041, doi:10.1029/93JB02107.

Wilson, D. S., et al. (2006), Drilling to gabbro in intact ocean crust, *Science*, *312*, 1016–1020, doi:10.1126/science.1126090.

Workman, R. K., and S. R. Hart (2005), Major and trace element composition of the depleted MORB mantle (DMM), *Earth Planet. Sci. Lett.*, *231*, 53–72, doi:10.1016/j.epsl.2004.12.005.

Zukin, J. H., and J. Francheteau (1990), A tectonic test of instantaneous kinematics of the Easter Microplate, *Oceanol. Acta*, *10*, 183–198.

D. S. Coleman, Department of Geological Sciences, University of North Carolina at Chapel Hill, Chapel Hill, NC 27599, USA.

J. A. Karson, Department of Earth Sciences, Syracuse University, Syracuse, NY 13244, USA.

E. M. Klein, Division of Earth and Ocean Sciences, Duke University, Durham, NC 27705, USA.

M. A. Pollock, Department of Geology, College of Wooster, Wooster, OH 44691, USA. (mpollock@wooster.edu)